Geological-petrophysical insights in the deep Cambrian dolostone reservoirs in Tarim Basin, China

Jin Lai, Shichen Liu, Yi Xin, Song Wang, Chengwen Xiao, Qiuqiang Song, Xu Chen, Kefu Yang, Guiwen Wang, and Xiujian Ding

ABSTRACT

Cores, thin sections, and cathodoluminescence analysis were integrated to document the occurrence and petrology of dolomites, and their pore systems in the Cambrian of Tarim Basin, China. Depositional facies, pore types, and dolomitization processes of various dolostone reservoir types are determined. Six types of dolomite are recognized, including microbial dolomite, dolomicrite, fabric-retentive dolomite, fabric-obliterative dolomite, fine to medium crystalline dolomite cement, and saddle dolomite cement. Pore systems are dominantly vugs, anhydrite dissolution pores, intercrystalline pores, intercrystalline dissolution pores, fabric dissolution pores, and microfractures. Four porous dolostone reservoirs include sabkha dolostone, seepage-reflux dolostone, burial dolostone, and hydrothermal dolostone. Fractures are an important factor in enhancing reservoir quality in dolostone reservoirs.

Conventional wire-line logs and image logs are calibrated with cores and related thin sections. Sabkha dolostone reservoirs are characterized by dark and bright spots on the image logs. Seepage-reflux dolostone reservoirs are related to high-energy depositional facies and are characterized by low gamma-ray amplitude, increasing sonic transit time and neutron porosity but reducing bulk density values. Evident dark spots (vugs) are recognized on image logs, and all three porosity logs suggest relatively high reservoir quality in burial dolostone reservoirs. Hydrothermal dolostone reservoirs are recognized by high gamma-ray response caused by hydrothermal minerals (fluorite), and porosity curves

Copyright ©2021. The American Association of Petroleum Geologists. All rights reserved.

Manuscript received May 30, 2019; provisional acceptance August 1, 2019; revised manuscript received September 24, 2019; revised manuscript provisional acceptance November 25, 2019; 2nd revised manuscript received January 13, 2020; 2nd revised manuscript provisional acceptance March 16, 2020; 3rd revised manuscript received March 31, 2020; 3rd revised manuscript provisional acceptance April 7, 2020; 4th revised manuscript received April 29, 2020; 4th revised manuscript provisional acceptance May 11, 2020; 5th revised manuscript received June 2, 2020; final acceptance January 26, 2021.
DOI:10.1306/03122119135

AUTHORS

JIN LAI ~ *State Key Laboratory of Petroleum Resources and Prospecting, China University of Petroleum (Beijing), Beijing, China; College of Geosciences, China University of Petroleum (Beijing), Beijing, China; sisylaijin@163.com*

Jin Lai graduated in 2010 with a B.S. degree in geological engineering and received his Ph.D. in geology from China University of Petroleum (Beijing) in 2016. He worked from 2015 to 2016 as a visiting scientist at the Bureau of Economic Geology, Jackson School of Geosciences, at The University of Texas at Austin. His current research interests include hydrocarbon reservoir characterization and well-log analysis. He has also worked extensively with numerous types of unconventional reservoirs, including tight gas sandstones and tight oil plays in the Ordos, Sichuan, and Tarim Basins, China. He is now an associate editor of *AAPG Bulletin*, *Petroleum Science*, and *Journal of Petroleum Science and Engineering*.

SHICHEN LIU ~ *State Key Laboratory of Petroleum Resources and Prospecting, China University of Petroleum (Beijing), Beijing, China; liushichen2006@163.com*

Shichen Liu graduated in 2019 with a B.S. degree in geological engineering, and he is now a postgraduate student majoring in geology. He is focusing on well-log analysis of deep dolomite reservoirs.

YI XIN ~ *Research Institute of Petroleum Exploration and Development, Tarim Oilfield Company, China National Petroleum Corporation (CNPC), Xinjiang, China; xinyi-tlm@petrochina.com.cn*

Yi Xin received his master's degree from Yangtze University in 2005 and his bachelor's degree from Jianghan Petroleum Institute in 2002. He is now a Ph.D. student at China University of Petroleum (Beijing). From 2005, he was employed at Tarim Oilfield Company, CNPC. He is a senior logging interpretation and evaluation engineer, mainly engaged in logging data processing and interpretation integrating new technologies with

Downloaded from http://pubs.geoscienceworld.org/aapgbull/article-pdf/105/11/2263/5431410/bltn19135.pdf
by China University of Geosciences Beijing user

conventional methods in tight gas sandstone and deep dolostone reservoirs.

SONG WANG ~ *State Key Laboratory of Petroleum Resources and Prospecting, China University of Petroleum (Beijing), Beijing, China; 603642162@qq.com*

Song Wang graduated in 2015 with a B.S. degree in geophysics and is now a Ph.D. student at the China University of Petroleum (Beijing). His current research interests include well-log analysis of carbonate reservoirs.

CHENGWEN XIAO ~ *Research Institute of Petroleum Exploration and Development, Tarim Oilfield Company, CNPC, Xinjiang, China; xiaocw-tlm@petrochina.com.cn*

Chengwen Xiao received his Ph.D. from China University of Petroleum (Beijing) in 2008 and his bachelor's degree in 1990 from Jianghan Petroleum Institute. From 1990, he was employed at Tarim Oilfield Company, CNPC. He is now the leader of the Institute of Geophysics at the Tarim Oilfield Company. He is a senior engineer engaged in logging data processing and interpretation integrating new well-log technologies in tight gas sands reservoirs and fractured-vuggy carbonate reservoirs.

QIUQIANG SONG ~ *Research Institute of Petroleum Exploration and Development, Tarim Oilfield Company, CNPC, Xinjiang, China; songqq-tlm@petrochina.com.cn*

Qiuqiang Song received his master's degree in 2013 and his bachelor's degree in 2010 from Yangtze University. From 2013, he was employed at Tarim Oilfield Company, CNPC. He is now a logging interpretation and evaluation engineer, mainly engaged in logging data processing and interpretation in fractured-vuggy carbonate reservoirs.

XU CHEN ~ *Research Institute of Petroleum Exploration and Development, Tarim Oilfield Company, CNPC, Xinjiang, China; chenxu1-tlm@petrochina.com.cn*

Xu Chen received his master's degree from China University of Petroleum (Beijing) in 2014 and his bachelor's degree from Yangtze University in 2010. From 2014, he was employed at Tarim Oilfield Company, CNPC. He is now an engineer engaged in log data

indicate good reservoir quality, which is supported by dark spots (vugs) on the image logs. Rapid decrease in resistivity, increasing in sonic transit time values, and the dark sinusoidal waves on the image logs are typical of fractured dolostone reservoirs. The distribution of dolostone reservoirs in each well is predicted using a comprehensive analysis of conventional and image logs, and they are calibrated with oil test data. The research provides insights in the analysis of genetic model of deeply buried dolostone reservoirs and establishes the predictable model for reservoir quality in dolostones via well logs.

INTRODUCTION

Dolostones are globally important hydrocarbon-bearing reservoir rocks and are attracting substantial and persistent interest because of their exploration potential (Warren, 2000; Ehrenberg et al., 2006; Roth et al., 2011; Nabawy, 2013; Wen et al., 2014; Bai et al., 2016; El Sharawy and Nabawy, 2016; Li et al., 2016; Aschwanden et al., 2019; Lai et al., 2019b; Pires et al., 2019; Jafari et al., 2020). Deeply buried Cambrian dolostone reservoirs are currently key exploration targets in the Tarim Basin of western China (Zhao et al., 2012, 2014; Wang et al., 2014; Jiang et al., 2016, 2018; Shen et al., 2016; Tian et al., 2018). Numerous studies have considered the tectonic evolution (Zhang et al., 2009; Du et al., 2018), depositional facies (Gao and Fan, 2015; Wang et al., 2018), dolomitization process (Jiang et al., 2016), diagenetic evolution (Li et al., 2016; Jiang et al., 2018), fluid alteration (Dong et al., 2013; Jiang et al., 2015), and petroleum geology (Zhu et al., 2015a, 2018) of the Cambrian dolostones in Tarim Basin.

Despite being deeply buried, hydrocarbon exploration has confirmed that abundant hydrocarbon resources are hosted in these ancient dolostone reservoirs (Wang et al., 2014; Jiang et al., 2016). The initial discovery well, Zhongshen (Zs) 1, was drilled in 2012 and tested gas from two zones. The lower Cambrian Xiaoerbulake Formation flowed gas at the rate of 30,000 m^3/day (1060 MCFGD) and 34 m^3/day (214 BWPD) water. The middle Cambrian Awatage Formation tested oil from perforations at the rate of 15.4 m^3/day (96 BOPD) and gas at the rate of 173–10,301 m^3/day (61–363 MCFGD) (Shen et al., 2016). In 2013, in the lower–middle Cambrian dolostone reservoirs of well ZS 1C, flowed natural gas at the rate of 158,545 m^3/day (5600 MCFGD) (drawdown pressure: 40 MPa [5800 psi]) was obtained (Wang et al., 2014; Zhu et al., 2016, 2018). Liquid hydrocarbons were also produced in well Zs 5, with a daily natural gas production of 11,804 m^3/day (417 MCFGD) and oil production of 24.17 m^3/day (152 BOPD) through a 6-mm choke after acid fracturing (He et al., 2016). Additionally, many other exploratory wells have discovered high-quality dolostones with pores and vugs

Downloaded from http://pubs.geoscienceworld.org/aapgbull/article-pdf/105/11/2263/5431410/bltn19135.pdf
by China University of Geosciences Beijing user

containing liquid hydrocarbon and natural gas in the deeply buried Cambrian dolostones (Zhu et al., 2015a).

Dolomite forms in various environmental settings and diagenetic conditions (Ngia et al., 2019) and is identified by significant heterogeneity at numerous scales (Mollajan and Memarian, 2016; Tian et al., 2019). The lack of clarity in geologically genetic models and lack of geophysical characterization methods hinder further exploration and production of the ancient dolostone reservoirs buried to 8000 m (Jiang et al., 2016; Tian et al., 2019). Although the total thickness of Cambrian–Lower Ordovician dolostones in the Tarim Basin is more than 1000 m (Zheng et al., 2013; Gao and Fan, 2015; Li et al., 2016), most of the dolostones have poor reservoir quality because of the deep burial and intense multiphase diagenetic modifications (Jiang et al., 2016; Li et al., 2016; Lu et al., 2017). Therefore, it is essential for successful exploration of the dolostone reservoirs and it is necessary to understand the origin and mechanisms that maintain high porosity in dolostones buried to such a great depth in Tarim Basin. Additionally, predicting porous dolostones using well-log data remains a challenging task.

The purpose of this study was to unravel the genetic models of various dolostone reservoirs through construction of well-log characterization methods via integration of cores, conventional well logs, and image logs, thus closing the gap between geological description and petrophysical characterization.

Specifically, the following two questions are addressed:

1. How many different types of dolostone reservoirs are there in Cambrian strata of the Tarim Basin, and what are their genetic models?
2. Can dolostone reservoirs be predicted using well logs?

GEOLOGICAL SETTING

The Tarim Basin, located in the southern part of the Xinjiang Province (Uygur Autonomous Region), is the largest petroliferous superposed basin in China, occupying an area of 56×10^4 km^2 (Figure 1) (Chen et al., 2000; Qiu et al., 2012; Jiang et al., 2015; Gao et al., 2016; Lai et al., 2017a). Several structural units (three uplifts: northern, central, and southern; and four depressions: the Kuqa, northern, southwestern, and southeastern) are present in the Tarim Basin because of a series of tectonic events (Caledonian, Hercynian, Indosinian, and Himalayan cycles) (Figure 1) (Jin et al., 2009; Zhang et al., 2009, 2018; Gao et al., 2015; Zhu et al., 2015a; Du et al., 2018; Guo et al., 2018; Ngia et al., 2019). From the Sinian to the Ordovician, the Tarim Basin was a large, shallow carbonate platform, and thick-bedded dolostones were deposited from the

processing and interpretation in carbonate reservoirs.

KEFU YANG ~ *Research Institute of Petroleum Exploration and Development, Tarim Oilfield Company, CNPC, Xinjiang, China; yangkf-tlm@petrochina.com.cn*

Kefu Yang received his master's degree from Southwest Petroleum University (SWPU) in 2015 and his bachelor's degree from SWPU in 2012. From 2015, he was employed at Tarim Oilfield Company, CNPC. He is now an engineer engaged in log data processing and interpretation in carbonate reservoirs.

GUIWEN WANG ~ *State Key Laboratory of Petroleum Resources and Prospecting, China University of Petroleum (Beijing), Beijing, China; College of Geosciences, China University of Petroleum (Beijing), Beijing, China; wanggw@cup.edu.cn*

Guiwen Wang received his Ph.D. in geology from China University of Petroleum (Beijing) in 2010 and both his B.S. and M.S. degrees from China University of Geosciences (Wuhan) (1987 and 1990). From 1991 to 1993, he was employed at the Research Institute of Tarim Petroleum Exploration and Production Headquarters, engaged in well-logging geology interpretation and new technique extension. He spent half a year as a visiting scientist at Queen's University, United Kingdom. He is the secretary of the College of Geosciences at China University of Petroleum (Beijing). He is now a professor and supervises graduate students and postdoctoral scholars. He has more than 30 years of experience working in petroleum exploration and development. His technical specialties and current research interests include well-logging geology, sedimentology, and reservoir geology. He is the corresponding author of this paper.

XIUJIAN DING ~ *Key Laboratory of Deep Oil & Gas, China University of Petroleum (East China), Qingdao, China; dingxj@upc.edu.cn*

Xiujian Ding received his bachelor's degree in geological engineering from China University of Petroleum (Beijing) in 2009 and his Ph.D. in geology from China University of Petroleum (Beijing) in 2014. He is now an associate professor at China University of Petroleum

Downloaded from http://pubs.geoscienceworld.org/aapgbull/article-pdf/105/11/2263/5431410/bltn19135.pdf
by China University of Geosciences Beijing user

(East China). His current research interest includes petroleum geology.

ACKNOWLEDGMENTS

This work is financially supported by the Natural Science Foundation of Beijing (8204069), Science Foundation of China University of Petroleum, Beijing (No. 2462021YXZZ003), the Fundamental Research Funds for the Central Universities, and the Opening Fund of Key Laboratory of Deep Oil & Gas (20CX02116A). The authors would like to express their sincere thanks to the PetroChina Tarim Oilfield Company for their assistance in providing the information and for their technical input to this work. This study is based on work carried out by a large group of participants. We thank the staff of the Research Institute of Petroleum Exploration and Development of PetroChina Tarim Oilfield Company. Heng Zhang is greatly acknowledged for providing data. The software GeoFrame and Techlog were used to produce the borehole images. We thank Hangzhou Institute of Geology, Research Institute of Petroleum Exploration and Development of PetroChina, for their work. This manuscript benefited from the critical but constructive comments of five reviewers. The authors thank the AAPG technical editors, Paula Sillman and Andrea Sharrer, for their kind work on this paper and AAPG Editor Robert K. Merrill for his enthusiasm, patience, and tireless efforts.

late Cambrian to the Early Ordovician (Gao and Fan, 2015; Hu et al., 2019; Lai et al., 2020).

The Cambrian can be subdivided into six formations from bottom to top, including the Yuertusi Formation (ϵ_1y), Xiaoerbulake Formation (ϵ_1x), Wusonggeer Formation (ϵ_1w), Sayilike Formation (ϵ_2s), Awatage Formation (ϵ_2a), and Qiulitage Formation (ϵ_3q) (Figure 2) (Gao and Fan, 2015; Jiang et al., 2016). Six third-order sequences (SQ1–SQ6) in the Cambrian are recognized through a combination of core and outcrop observation and well-log and seismic-based facies analysis (Jiang et al., 2018). The lower Cambrian (ϵ_1x and ϵ_1w) is composed mainly of dolomite, the middle Cambrian (ϵ_2s and ϵ_2a) is dominated by evaporite-bearing sequences (anhydrites, dolomites, and mudstones), and the Upper Cambrian (ϵ_3q) consists mainly of an approximately 600-m-thick dolomite (Zhang et al., 2009). From west to east, the depositional facies of the Cambrian–Ordovician formations are recognized as large shallow carbonate platform, slope facies (limestone and marlstone), and basinal facies (mudstone and shale) (Du et al., 2018).

The burial and geothermal history reconstruction was based on the work of Cai et al. (2001). Cambrian strata had been rapidly buried to a depth of 4000 m during late Ordovician and subsequently continuously buried to a maximum depth of 7000 m or deeper, reaching maximum temperatures of >180°C (>356°F) (Figure 3). Hydrocarbons migrating from the lower to middle Cambrian and Middle to Upper Ordovician source rocks accumulated in the Ordovician carbonates (Pang et al., 2013). Ordovician strata are mainly composed of limestones, and only the Lower Ordovician Penglaiba Formation contains dolostones (Dong et al., 2013; Zhang et al., 2018; Fu, 2019). The underlying lower Cambrian, basin-wide distributed mudstones and black shales are the main source rocks for the overlying dolostone reservoir. The organic matter is dominated by type I and II_1 kerogens, with total organic carbon ranging between 1.0 and 3.0 wt. % and vitrinite reflectance greater than 1.5% (Cai et al., 2015; Jiang et al., 2018). Abundant oil and gas was generated in the Cambrian ϵ_1*y* source rocks (Zhu et al., 2018). Active faults and fractures act as the hydrocarbon migration pathways from lower Cambrian source rocks into the overlying Cambrian and Ordovician dolomite reservoirs (Jiang et al., 2015).

DATA AND METHODS

A total of 200 core plugs (mostly dolostones) were taken from cores in wells Zs 5, Hetian 2, Chutan 1, Shutan 1, Madong (Md) 5, Md 8, Zhonggu (Zg) 5, Zg 582, Zg 58, Zg 61, Luosi 2, and Zhonghan 1 (Zh) 1. Routine core analysis (porosity and permeability) was conducted on the plug samples 2.5 cm in diameter and 5 cm in length). Before thin-section preparation, blue or red fluorescent epoxy was impregnated into rock samples to aid in identifying pores and

Downloaded from http://pubs.geoscienceworld.org/aapgbull/article-pdf/105/11/2263/5431410/bltn19135.pdf
by China University of Geosciences Beijing user

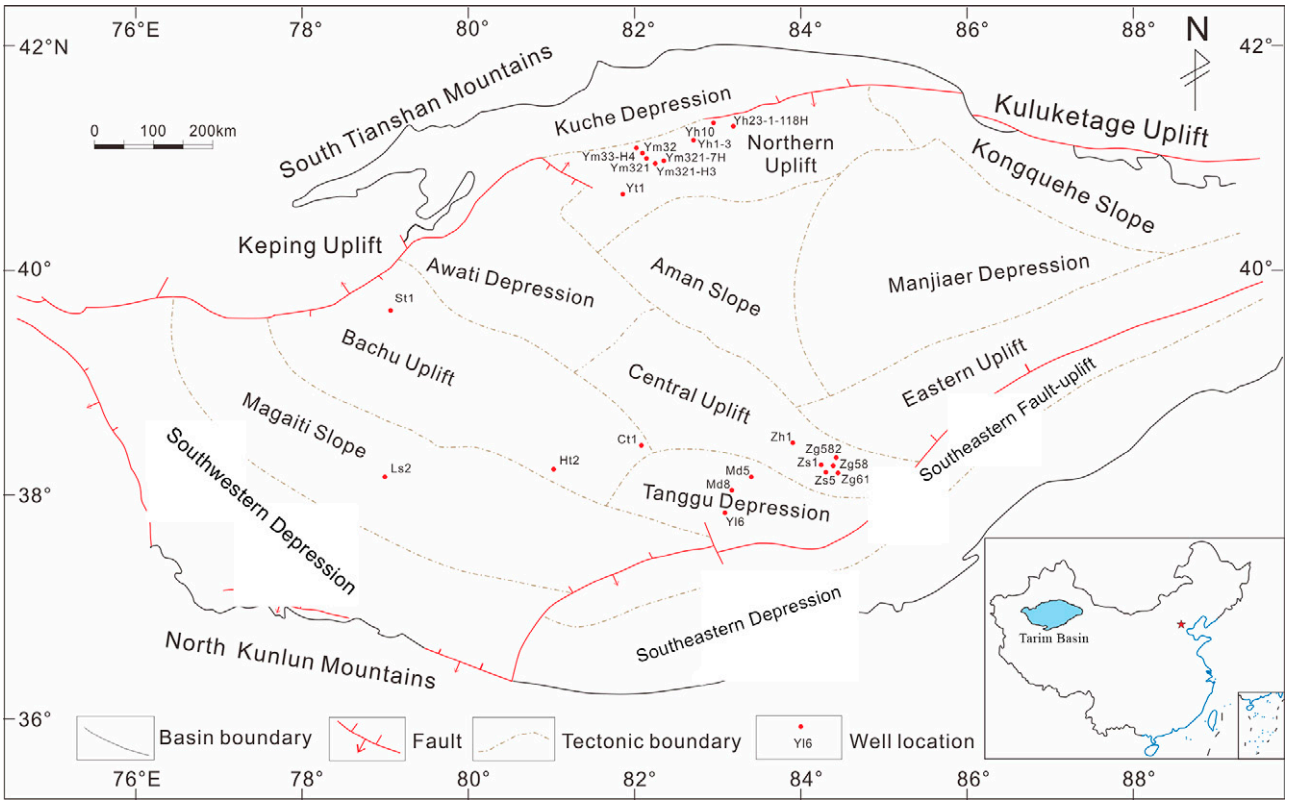

Figure 1. Structural division map of the Tarim Basin within China (Gao et al., 2015; Gao and Fan, 2015; Jiang et al., 2016). Ct = Chutan; Ht = Hetian; Ls = Luosi; Md = Madong; Y = Ya; Yh = Yaha; Ym = Yingmai; Yt = Yingtan; Zg = Zhonggu; Zh = Zhonghan; Zs = Zhongshen.

microfractures. Thin sections (0.03 mm in thickness) were stained with Alizarin Red S and potassium ferricyanide to differentiate between calcite (Fe-calcite) and dolomite. All thin sections were examined by optical transmitted light and cathodoluminescence (CL) microscopy.

Conventional well-log data include natural gamma ray (GR), caliper (CAL), spontaneous potential, lithodensity, deep resistivity, shallow resistivity, bulk density (DEN), neutron porosity (CNL), and acoustic porosity (AC). Fullbore formation microimager (FMI) and extended-range microimager (XRMI) imager tool was used to acquire the high-resolution images of the boreholes. The FMI or XRMI tool has two perpendicular pairs of CAL arms, and each arm hosts a pad and attached flap, and 24–25 electrodes are located on each of the eight or six pads (Rajabi et al., 2010; Folkestad et al., 2012; Brekke et al., 2017; Nian et al., 2018). Therefore, a total of 192 or 150 microresistivity curves can be recorded during logging, and the microresistivity fluctuations around the borehole wall provide important information for geological interpretation of logged intervals (Folkestad et al., 2012; Brekke et al., 2017; Lai et al., 2018b). Structural characteristics (borehole breakout, fractures, faults), lithology, and sedimentary structures can be identified on the images (Xu et al., 2009; Folkestad et al., 2012; Khoshbakht et al., 2012; Nian et al., 2017; Lai et al., 2018b).

RESULTS

Occurrence and Petrology of Dolomites

The Cambrian–Lower Ordovician in the Tarim Basin is primarily composed of dolostones (Gao and Fan, 2015; Zhu et al., 2015a, b). The Lower Ordovician Penglaiba Formation consists of massive dolostones interbedded with minor limestone layers in the upper part, whereas the Cambrian strata are dominantly composed of dolomite based on the observations of Keping field outcrops and well cores (hand specimen and thin sections) (Zhu et al., 2015a; Jiang et al., 2016; Hu et al., 2019). The Cambrian dolostones include dolomicrite (Figure 4A), dolograinstone

Downloaded from http://pubs.geoscienceworld.org/aapgbull/article-pdf/105/11/2263/5431410/bltn19135.pdf
by China University of Geosciences Beijing user

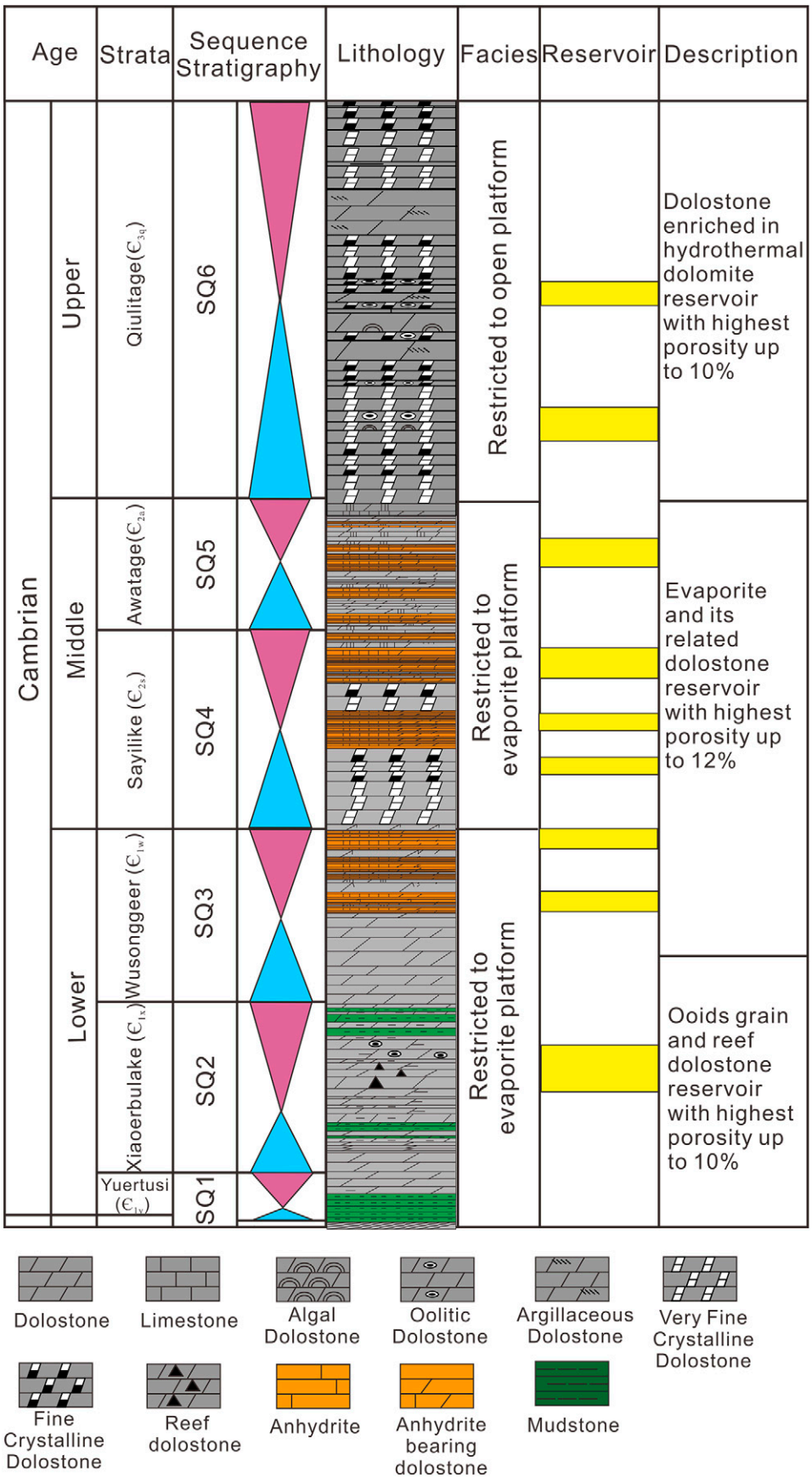

Figure 2. The sequence (SQ) stratigraphy, lithology association, and reservoir description of the Cambrian strata in the Tarim Basin (Jiang et al., 2018).

Downloaded from http://pubs.geoscienceworld.org/aapgbull/article-pdf/105/11/2263/5431410/bltn19135.pdf
by China University of Geosciences Beijing user

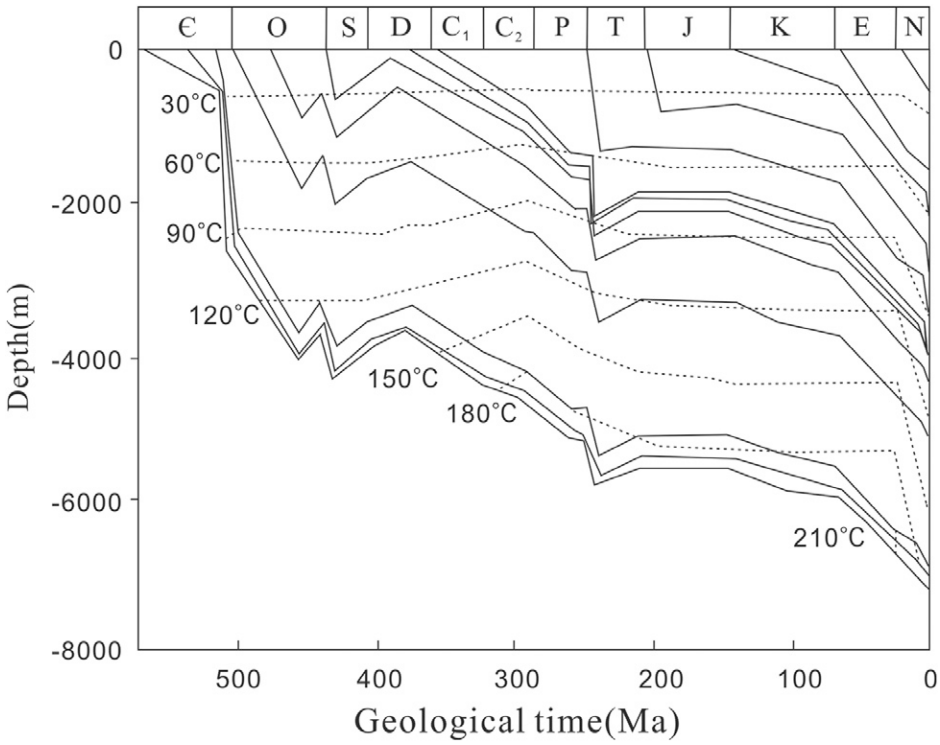

Figure 3. The reconstructed burial and geothermal history of well Tacan 1 in Tazhong uplift (Cai et al., 2001). Є = Cambrian; C_1 = early Carboniferous; C_2 = late Carboniferous; D = Devonian; E = Paleogene; J = Jurassic; K = Cretaceous; N = Neogene; O = Ordovician; P = Permian; S = Silurian; T = Triassic.

(ooid grains, intraclasts, etc.) (Figure 4B), and crystalline dolostone (very fine, fine-medium-coarse crystalline dolostone) (Figure 4C, D), as well as microbial dolostones (Zhu et al., 2015b; Jiang et al., 2016; Ngia et al., 2019). The fine crystalline dolostones are dark gray to brown-gray in color, whereas the medium-to-coarse crystalline dolostones are pale brown and light gray (Figure 4) (Zhu et al., 2015a). Gypsum nodules are common in the crystalline dolostone (Figure 4E), and some of the grain dolostones (dolograinstone) and crystalline dolostones contain abundant vugs (enlarge dissolution pores) (Figure 4F) (Jiang et al., 2016; Ngia et al., 2019; Lai et al., 2020).

Petrographic observation and CL analysis indicates that there are six types of dolomites (including four types of matrix dolomite, one cement dolomite, and one saddle dolomite). These are recognized in terms of crystal size and presence of grains: (1) microbial dolomite (D1) (Figure 5A, B), (2) dolomicrite or very finely crystalline dolomite (D2) (Figure 5C), (3) fabric-retentive dolomite (D3) (Figure 5D), (4) fabric-obliterative (crystalline) dolomite (D4) (Figure 5E, F), (5) finely to medium crystalline cement dolomite (Cd) (Figure 5G), and (6) saddle dolomite cements (Sd) (Figure 5H) (Dong et al., 2013; Zhu et al., 2015a; Jiang et al., 2016; Du et al., 2018; Lai et al., 2020). Matrix dolomites are dominated by fine to medium and coarse crystalline dolomite (Zhu et al., 2015b). Many dolostones are composed of multiple types of dolomite according to field and microscopic observations (Zhu et al., 2015a; Du et al., 2018; Hu et al., 2019).

The D1 dolomites (algal-laminated) are mainly found in the Keping-Bachu uplift of the Tarim Basin (Figure 5A, B) (Zheng et al., 2013; Hu et al., 2014; Huang et al., 2014; You et al., 2014; Jiang et al., 2016; Wang et al., 2018; Ngia et al., 2019). The D2 dolomite (dolomicrite) is commonly associated with anhydrite, and under low magnification of petrographic observations, the primary sedimentary fabric of precursor limestones can be identified (Figure 5C) (Du et al., 2018). The D2 dolomites, which are near-micritic crystals, are the predominant dolomite in low-energy, restricted facies (Jiang et al., 2016). The D3 dolomite (fabric-retentive) implies high-energy depositional facies (oolitic shoal and reef facies), in which the primary fabrics (ooids, intraclasts) are fuzzy but visible by petrographic observation (Figure 5D) (Jiang et al., 2016). The D4 dolomite (fabric-obliterative) is characterized

Downloaded from http://pubs.geoscienceworld.org/aapgbull/article-pdf/105/11/2263/5431410/bltn19135.pdf
by China University of Geosciences Beijing user

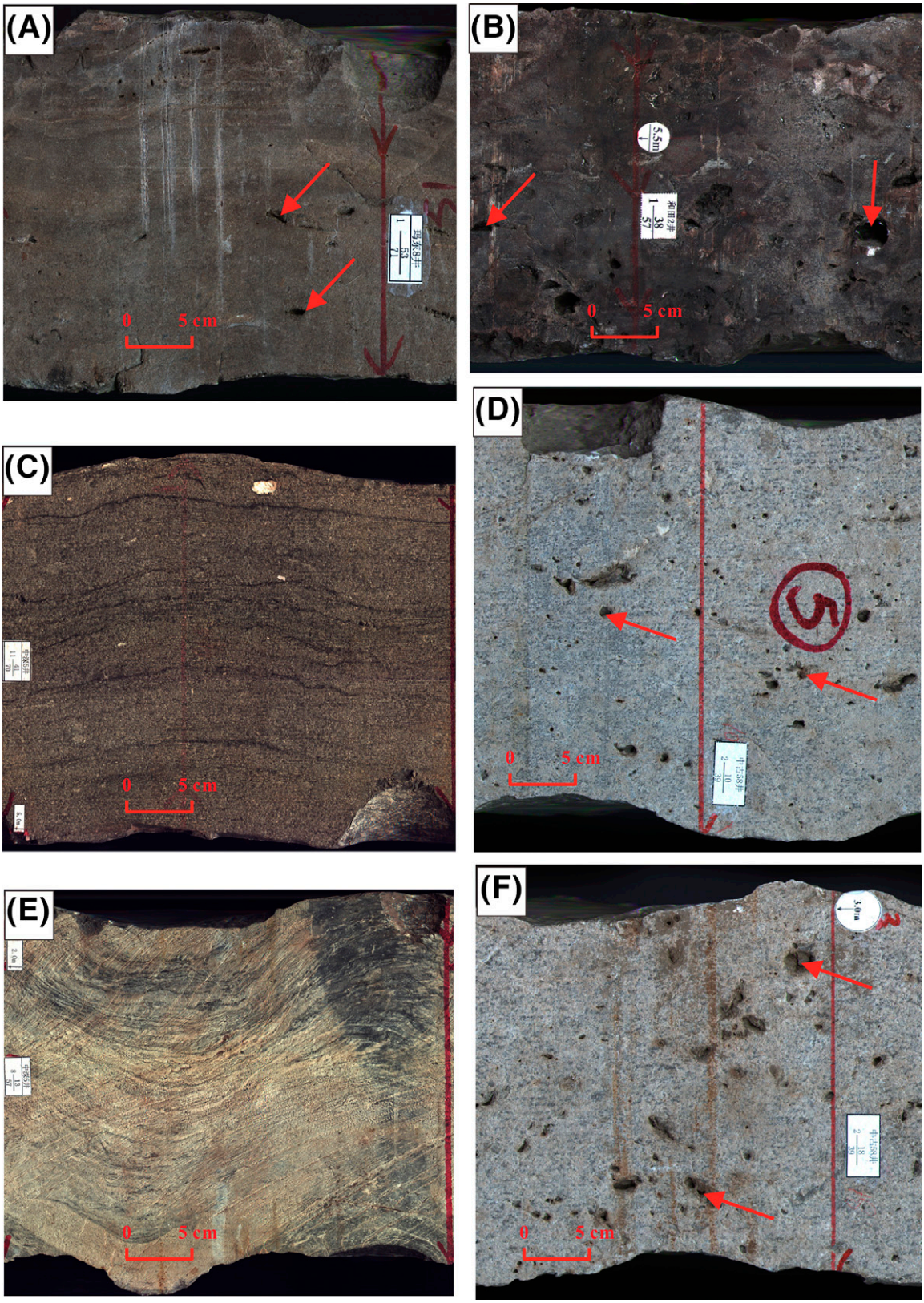

Figure 4. Core data showing the various types of dolostones. Note the pore spaces (red arrows). (A) Dolomicrites, well Madong 8, 4786.2 m, Cambrian Xiaqiulitage Formation ($\epsilon_3$xq). (B) Intraclast dolostones, well Hetian 2, 6495.44 m, ϵ. (C) Fine crystalline dolostone, well Zhonggu (Zg) 5, 6224.38 m, ϵ. (D) Fine crystalline dolostone, well Zg 58, 3610.49 m, $\epsilon_3$xq. (E) Gypsum bearing fine crystalline dolostone, well Zg 5, 6545.44 m, ϵ. (F) Vugs in the crystalline dolostone, well Zg 5, 6189.76 m, ϵ.

Downloaded from http://pubs.geoscienceworld.org/aapgbull/article-pdf/105/11/2263/5431410/bltn19135.pdf
by China University of Geosciences Beijing user

by fine to medium-to-coarse crystalline dolomite rhombs (Figure 5E), in which the primary fabric is indiscernible and fully destroyed by intense recrystallization or replacement during burial diagenesis (Figure 5F). The dolomite crystals generally exhibit crystal mosaics with curved crystal surfaces (Du et al., 2018). The Cd grow into open pores or are filling in fractures (Figure 5G). The Sd have planar subhedral to nonplanar anhedral textures, and they occur as filling in vugs, fractures, or matrix replacement (Figure 5H) (Du et al., 2018). Saddle dolomites are closely related to a regional hydrothermal event.

Pore Systems

The Cambrian dolostones contain various pore types (Zhu et al., 2015b; Li et al., 2016; Jiang et al., 2018; Lai et al., 2020). Vugs, which are easily detected by core observation (Figure 4F), are also apparent in thin-section petrography and occur as irregular dissolution-enlarged interparticle pores (Figure 6A). The gypsum (anhydrite)-bearing dolostones contain anhydrite dissolution pores, in which the gypsum (anhydrite) was almost completely dissolved. In some cases, there are gypsum remnants within the dissolution pores, especially in the northern uplift of Tarim Basin (Figure 6B) (Zheng et al., 2012; Shen et al., 2015, 2016; Zhao et al., 2015; Lai et al., 2020). The anhydrite dissolution pores significantly enhance porosity in the evaporite-bearing dolostones (Jiang et al., 2018). However, gypsum (anhydrite) also occurs as beds or nodules (Figure 4E), or even pore-filling cements, and in some cases completely fills the pore space (Jiang et al., 2016). None of the beds and nodules are leached in the Cambrian dolostones in the Tazhong uplift. In well Zs 5, the gypsum nodules significantly reduce the intergranular pore volume (Figure 6C, D).

Various amounts of intercrystalline porosity (polygonal) are seen in the crystalline dolomite because of various degrees of dolomitization (Figure 6E), and additionally, dissolution sometimes occurs along the intercrystalline pore boundaries creating intercrystalline dissolution pores (Figure 6F). The fine to medium crystalline dolomite, with lighter color, commonly has higher porosity than dolomicrite or very finely crystalline dolostones because of their abundance in intercrystalline pores (Zhu et al., 2015a; Li et al., 2016). Abundant intercrystalline pores were detected under the microscope in the medium-to-coarse dolostones (Figures 5F, 6E). Most of the porous dolostones in the Tarim Basin contain intercrystalline porosity (Jiang et al., 2018). In some cases, the fabrics (ooids and intraclasts) may be leached, forming fabric dissolution pores (Figure 6G, H). Microfractures (open) are also important pore spaces in the Cambrian dolostones (Figure 6I). However, dolomite, calcite, silica, and fluorite cements may fill the pore space (Figure 6J) (Lai et al., 2020).

DISCUSSION

Genetic Types of Porous Dolostone Reservoirs

The Cambrian dolostones are deeply buried (3500–8000 m) (Jiang et al., 2018), and the reservoir quality is poor because of various diagenetic changes (intensive compaction, as well as cementation by calcite, gypsum, dolomite, and quartz) (Jiang et al., 2016; Li et al., 2016). Therefore, the secondary porosity created by leaching and fracturing is an important factor creating porosity in the deeply buried dolomite reservoirs (Jin et al., 2009; Jiang et al., 2016; Li et al., 2016). Dissolution in dolostones can be associated with early, near-surface diagenetic processes and subaerial exposure, related meteoric water dissolution, and hydrothermal fluids under deep burial conditions or thermochemical sulfate reduction (TSR) (Loucks, 1999; Worden et al., 2000; Wierzbicki et al., 2006; Jiang et al., 2014, 2016, 2018; Zhu et al., 2015a; Li et al., 2016). The carbon, oxygen, and strontium isotope compositions as well as fluid inclusion data all confirm that two types of fluids (including meteoric water and hydrothermal fluid) have affected the lower Paleozoic dolomite reservoirs in the Tarim Basin (Zhu et al., 2015a). However, abundant intercrystalline porosity was created in the fine to medium crystalline dolostones because of multiphase dolomitization (Jiang et al., 2016; Lai et al., 2019a). Therefore, there are some porous dolostone reservoirs with high porosity in the Cambrian dolostones despite their deep burial and old geological age (Zhao et al., 2014; Jiang et al., 2016; Li et al., 2016; Zhu et al., 2018; Ngia et al., 2019).

Four types of porous dolostone reservoirs—sabkha, seepage-reflux, burial, and hydrothermal—are recognized according to their genetic (dolomitization and dissolution) models identified from thin-section

Downloaded from http://pubs.geoscienceworld.org/aapgbull/article-pdf/105/11/2263/5431410/bltn19135.pdf
by China University of Geosciences Beijing user

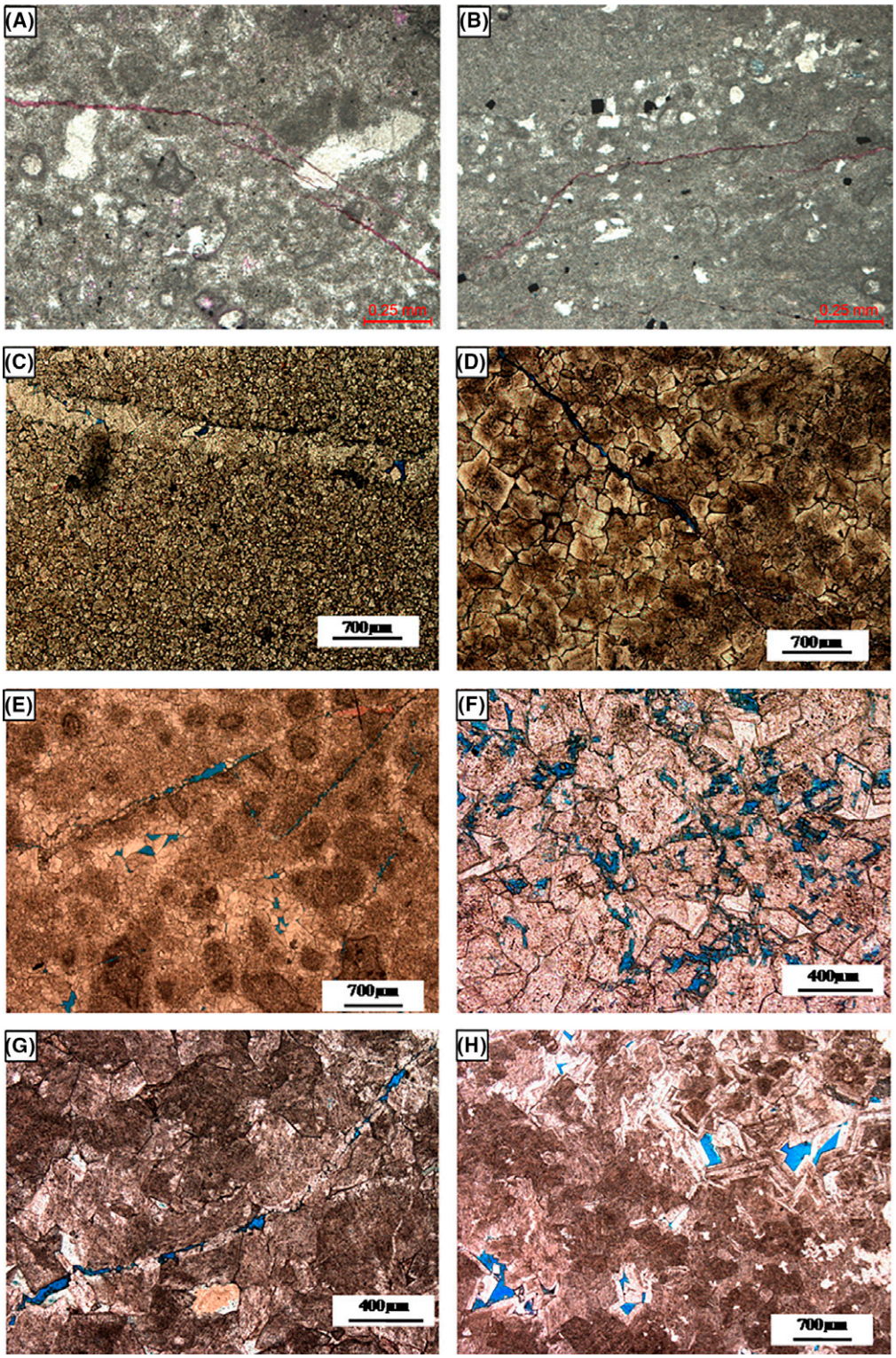

Figure 5. Thin-section images showing the various types of dolomites (You et al., 2013; Hu et al., 2014). (A) Microbial dolomite, Cambrian (Є), well Shutan (St) 1. (B) Microbial dolomite, Є, well St 1. (C) Very finely crystalline dolomites, well Hetian (Ht) 2, 39 5045 m, Cambrian Xiaoerbulake Formation. (D) Fabric-retentive dolomite (D2), well Ht 2, 5075 m, Є. (E) The D2, well Zhonggu (Zg) 582 3626.98 m, Є. (F) Fabric-obliterative dolomite, well Zg 61, 3549.51 m, Є. (G) Finely to medium crystalline dolomite cement filling in the fractures, Madong (Md) 8 4786.27 m, Є. (H) Saddle dolomite cements, well Md 8, 4787.13 m, Є.

Downloaded from http://pubs.geoscienceworld.org/aapgbull/article-pdf/105/11/2263/5431410/bltn19135.pdf
by China University of Geosciences Beijing user

petrography, CL analysis, and isotopic composition (Zhao et al., 2012, 2014; Zheng et al., 2012; Shen et al., 2016; Du et al., 2018).

Sabkha Dolostone Reservoirs

Anhydrite dissolution pores predominate in sabkha dolostone reservoirs. Related lithologies are evaporite-bearing dolomicrite or very finely crystalline dolostone (Table 1) deposited in a restricted lagoonal and tidal-flat environment (Zheng et al., 2012; Zhao et al., 2014; Jiang et al., 2016; Shen et al., 2016). Anhydrite is common in these low-energy, restricted environments (Jiang et al., 2016). Abundant anhydrite significantly decreases porosity (Jiang et al., 2018) and will likely be transformed into gypsum during burial. Exposure and intrusion of meteoric water will cause depositional anhydrite to dissolve, forming anhydrite dissolution porosity. The sabkha dolomites display nonluminescent or dull-red color patterns under CL (Figure 7A), suggesting that the dolomitization is syndepositional (early meteoric diagenesis) (Jiang et al., 2018). The $\delta^{13}C$ and $\delta^{18}O$ values (Vienna Peedee belemnite [VPDB]) of the sabkha dolomites are negative but not depleted. This suggests a subaerial exposure and meteoric water percolation, in other words, the sabkha capillary zone dolomitization model (Figure 8) (Zhao et al., 2012, 2014; Zheng et al., 2013; Jiang et al., 2016).

Seepage-Reflux Dolostone Reservoirs

Seepage-reflux dolostone reservoirs are dominantly grain dolostone and crystalline dolostone, which include D3 and D4 dolomites (Table 1). The pore systems are fabric (algal) selectively dissolution pores (Figure 9A). The seepage-reflux dolostone reservoirs were likely deposited in high-energy environments (platform margin: shoal and reef facies) (Jiang et al., 2016). The seepage-reflux dolomites exhibit dull-red to orange color patterns under CL (Figure 7B), implying that dolomitization occurred at shallow burial environments. The positive carbon composition and relatively heavy oxygen composition of the dolostones support reflux dolomitization (Figure 8) (Zhao et al., 2012, 2014; Zheng et al., 2013; Jiang et al., 2018). In arid climates, the evaporitic brine percolates into the underlying porous carbonates and dolomitizes limestone under shallow burial conditions (Jones and Xiao, 2005; Moore and Wade, 2013; Jiang et al., 2018)

Burial Dolostone Reservoirs

Burial dolostone reservoirs also include D4 and crystalline (medium-to-coarse crystalline) dolomite (Figure 9B; Table 1). Fabric (ooid and intraclasts)-enlarged dissolution pores (vuggy pores) (Figure 6G, H) as well as the intercrystalline (dissolution) pores (Figures 5F, 6E) are the predominant pore systems in burial dolostone reservoirs. Fabric-enlarged dissolution pores are commonly formed during seepage-reflux stage near the surface (Figure 6G, H). The pores formed in the seepage-reflux stage are further altered by burial dissolution, forming enlarged vugs (Figure 6G, H). In addition, the dolomites with cloudy cores but clear rims are typical of burial dolostone reservoirs (Figure 9B). Elevated temperatures at depth promote burial dolomitization (Haas et al., 2014; Jiang et al., 2016). Intense recrystallization or replacement during progressive burial obliterates the primary fabric (Jiang et al., 2016), and this type of dolostone reservoir generally has dull-red to red CL patterns (Figure 7C). The presence of fabric dissolution pores are considered to be inherited from dissolution pores formed during shallow burial.

Six third-order sequences (SQ1–SQ6) were recognized in the Cambrian strata (Jiang et al., 2018). Meteoric dissolution leads to the formation of dissolution pores (Zhu et al., 2015a), and these dissolution pores can be preserved as the dolomite is buried. In addition, burial-related dissolution as well as TSR can also enhance porosity (Jiang et al., 2016). Recrystallization during subsequent burial and elevated temperatures result in a depleted $\delta^{18}O$ VPDB value (Li et al., 2016); therefore, burial dolostone reservoirs are characterized by depleted $\delta^{18}O$ values (Figure 8) (Zhao et al., 2012, 2014; Zheng et al., 2013; Jiang et al., 2016) (Table 1).

Hydrothermal Dolostone Reservoirs

Saddle dolomite filling fractures and vugs are typical of hydrothermal dolostone reservoirs (Figure 5H) (Jiang et al., 2016). The presence of saddle dolomite is closely related to a regional hydrothermal event (high temperature conditions) (Al-Aasm et al., 2002; Zhang et al., 2009; Jiang et al., 2016). The lowest $\delta^{18}O$ values support this interpretation (Figure 8) (Zhang et al., 2009; Zhao et al., 2012, 2014; Zheng et al., 2013). Additionally, fluorite minerals fill the dissolution pores and fractures, which is typical of hydrothermal dolostone reservoirs (Figure 9C) (Table 1). The host dolomite is dissolved by hydrothermal fluids, resulting in

Downloaded from http://pubs.geoscienceworld.org/aapgbull/article-pdf/105/11/2263/5431410/bltn19135.pdf
by China University of Geosciences Beijing user

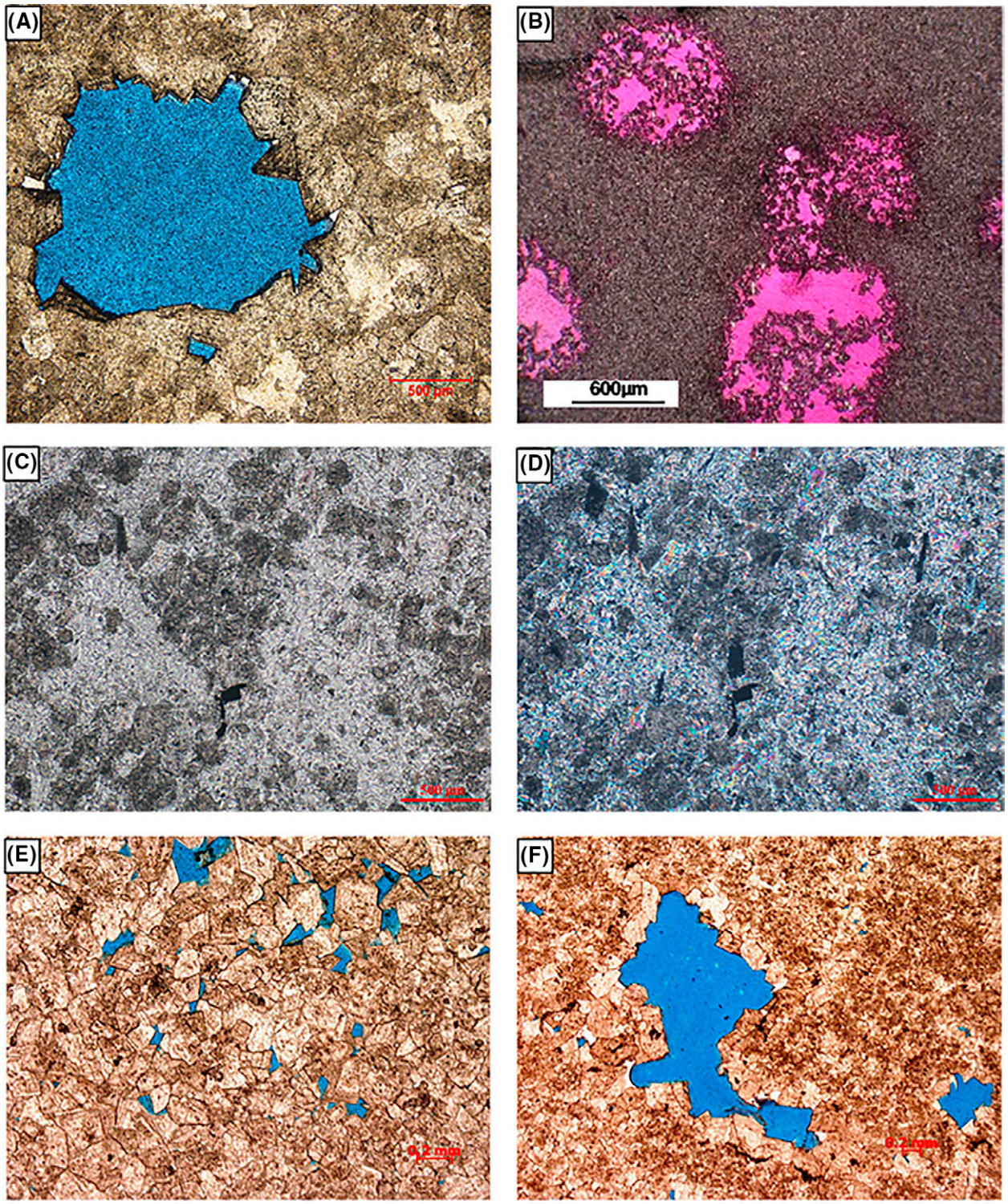

Figure 6. Thin section showing the pore systems in dolostones. (A) Dissolution-enlarged interparticle pores (vugs), well Zhonggu (Zg) 58, 3708.9 m, Cambrian (Є). (B) Dissolution pores in gypsum-bearing dolostones, well Yaha 10. (C) Gypsum nodules filling the pore volumes, well Zhongshen (Zs) 5, 6543.9 m, Є. (D) The same field view of (C) under the cross-polarized light. (E) Intercrystalline pores in the fine crystalline dolostones, well Zg 61, 3548.41 m, Є. (F) Intercrystalline dissolution pores, well Zg 61, 3548.76 m, Є. (G) Fabric dissolution pores, well Chutan 1, 7770.25 m, Є. (H) Fabric dissolution pores, well Madong (Md) 8, 4785.28 m, Є. (I) Microfractures, well Md 8, 4783.72 m, Є. (J) Calcite, silica, and fluorite cements fill the pores and microfractures, well Md 8, 4786.4 m, Є.

Downloaded from http://pubs.geoscienceworld.org/aapgbull/article-pdf/105/11/2263/5431410/bltn19135.pdf
by China University of Geosciences Beijing user

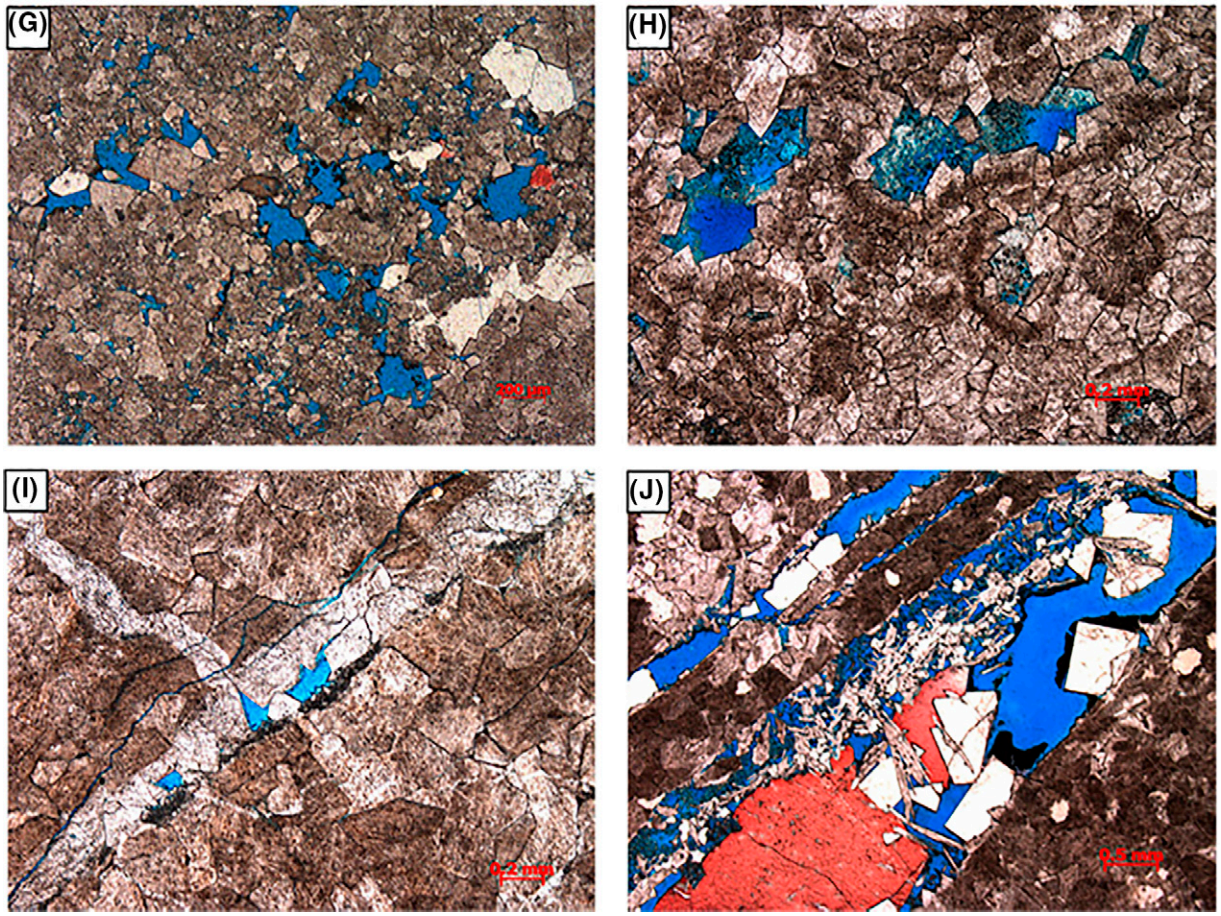

Figure 6. Continued.

secondary porosity (intercrystalline dissolution pores, hydrothermal-related, large dissolution pores, and fracture-enlarged pores) (Figure 9D), as well as the precipitation of Sd (Zhang et al., 2009; Zhu et al., 2015b). Saddle dolomites typically display bright orange CL patterns (Figure 7D). Hydrothermal fluids migrate up through faults and fractures (Jiang et al., 2015; Zhu et al., 2015b), and carbonates near the faults are dissolved, and limestones dolomitized (Iapponi et al., 2014; Jiang et al., 2015). Enlarged dissolution along the fractures is common (Figure 9E), and calcite, quartz, saddle dolomite, and fluorite are precipitated (Figures 6J, 9C).

Fractured Reservoirs

Fractures are important and enhance reservoir quality (Aghli et al., 2020). If effective fractures are developed, the four types of dolostone can develop into fractured dolostone reservoirs. Abundant microfractures are detected by thin-section petrography (Figures 6I, J; 9E, F). Cambrian dolomites experienced multiple episodes of intense tectonic activity during the Caledonian, Hercynian, Indosinian, and Himalayan orogeny events (Jin et al., 2009; Zhang et al., 2009, 2018; Zhu et al., 2015b; Ngia et al., 2019). Many faults and fractures form in deep dolostone reservoirs during multiphase tectonic activity, and the presence of fractures greatly enhances porosity and permeability of the deep dolostone reservoirs (Zhu et al., 2015b; Lai et al., 2021). Additionally, fractures as well as faults can act as the conduits along which dolomitizing fluids flow (Warren, 2000; Wilson et al., 2007; Zhang et al., 2009; Zhu et al., 2015b; Lyu et al., 2017). The fault or fracture-related fluids are responsible for the formation of hydrothermal dolostone reservoirs, and the Sd (Guo et al., 2016), forming fractured hydrothermal dolostone reservoirs (Luczaj et al., 2006). However, the fractures also contribute to dissolution, and dissolution-enlarged pores are common along the fractures, which can be seen in thin section (Figure 9E, F).

Downloaded from http://pubs.geoscienceworld.org/aapgbull/article-pdf/105/11/2263/5431410/bltn19135.pdf
by China University of Geosciences Beijing user

Downloaded from http://pubs.geoscienceworld.org/aapgbull/article-pdf/105/11/2263/5431410/bltn19135.pdf
by China University of Geosciences Beijing user

Table 1. Genetic Models and Characteristics of Various Types of Porous Dolostone Reservoirs

Reservoir Types	Depositional Facies	Lithology	Pore Spaces	CL Patterns	Isotope Compositions	Genetic Model	Well-Log Responses
Sabkha dolostones	Restricted lagoonal and tidal-flat facies	Evaporite-bearing dolomicrite or very finely crystalline dolostones	Anhydrate dissolution	Dull or none	Heavy $\delta^{13}C$ and $\delta^{18}O$	Sabkha dolomitization, meteoric water	Dark and bright spots; low GR, fluctuated resistivity, low bulk density
Seepage-reflux dolostones	Restricted platform margin: shoal and reef facies	Dolograinstone and crystalline dolostones	Fabric selectively dissolution pores	Dull-red to orange	Positive $\delta^{13}C$ and heavy $\delta^{18}O$	Reflux dolomitization, meteoric water	Dark spots; low GR, low bulk density, high CNL, medium-high resistivity
Burial dolostones	Shoal and reef facies	Dolograinstone and crystalline dolostones	Fabric (ooid and intraclasts) -enlarged dissolution pores and intercrystalline (dissolution) pores	Dull-red to red, orange	Depleted $\delta^{18}O$ values	Burial-related dissolution, TSR	Dark spots; low GR, high AC values, high CNL values but low bulk density
Hydrothermal dolostones	High- or low-energy facies	Dolograinstone and crystalline dolostones	Large pores, intercrystalline dissolution pores, and vugs	Bright orange	Lowest $\delta^{18}O$ values	Hydrothermal activities near faults or unconformities	Dark spots and sine waves; high GR, high CNL, low bulk density, low resistivity

See Zhao et al. (2012, 2014); Zheng et al. (2012); Jiang et al. (2016); Shen et al. (2016); and Du et al. (2018).
Abbreviations: AC = acoustic porosity; CL = cathodoluminescence; CNL = neutron porosity; GR = gamma ray; TSR = thermochemical sulfate reduction.

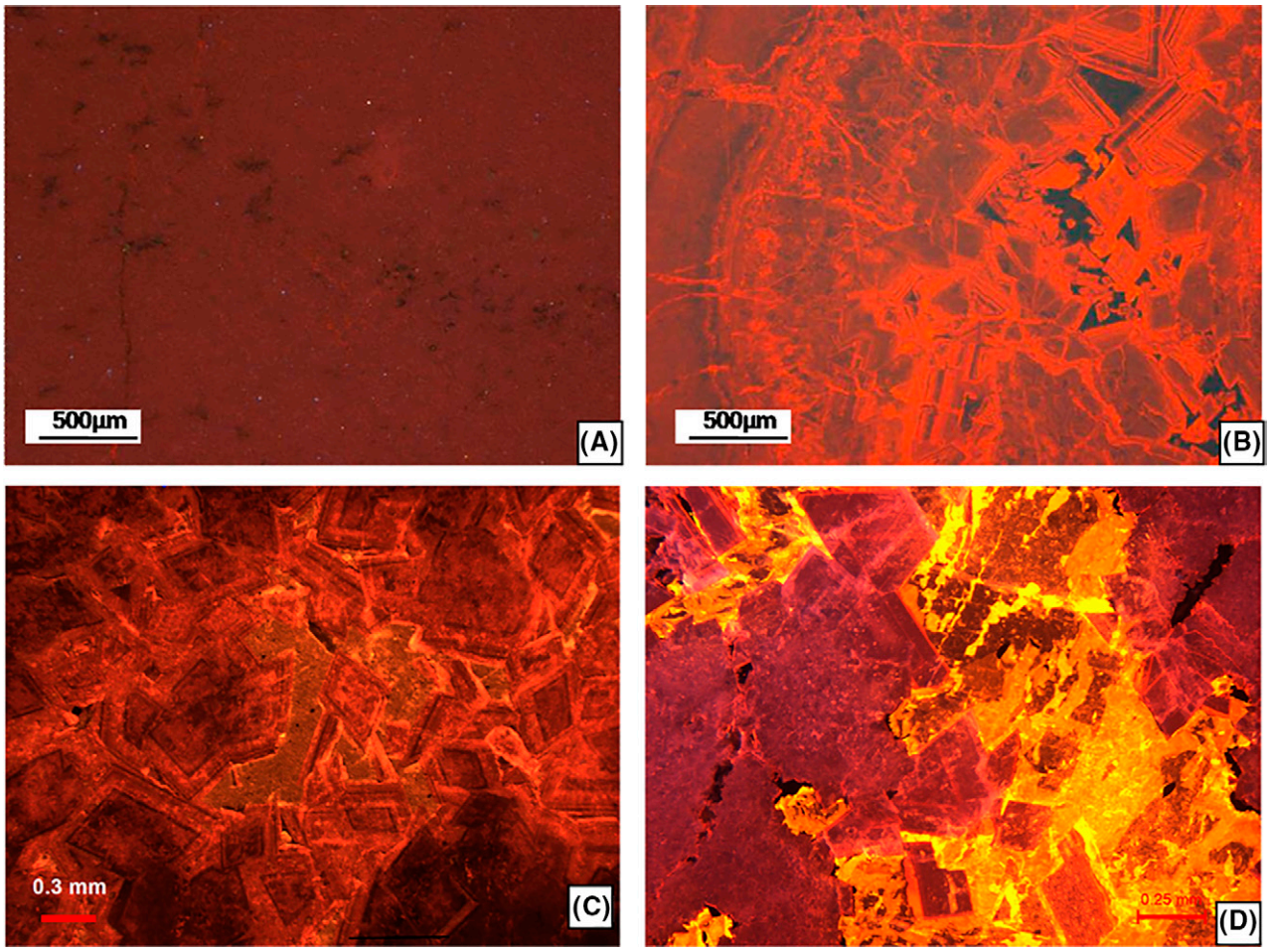

Figure 7. Cathodoluminescence (CL) photomicrographs showing different kinds of dolostone reservoirs in the Tarim Basin. (A) Sabkha dolostone reservoirs, well Tazhong 1, 4305.40 m (Zhao et al., 2012). (B) Seepage-reflux dolomites showing dull-red CL patterns. (C) Burial dolostone reservoirs, well Ma 2, 2317.60 m (Zhao et al., 2014). (D) Saddle dolomites showing bright orange, Chutan 1.

Geologically Genetic Model

The sabkha dolostone reservoirs are associated with the evaporite-enriched dolomicrite or very fine crystalline dolostone deposited in supratidal environments (Jiang et al., 2018). Leaching by meteoric water created anhydrite dissolution pores (selective dissolution) shortly after burial (Figure 6B) (Zhu et al., 2015a). The anhydrite-bearing precursor limestones below (third-order) sequence stratigraphic boundaries were exposed at the surface and experienced meteoric water dissolution (Zhao et al. 2014; Zhu et al., 2015a). Consequently, the anhydrite dissolution pores formed, and these pores were preserved during burial (Figure 10) (Zhu et al., 2015a). Meteoric dissolution can also be caused by regional uplift and karstification, which will result in the formation of anhydrite dissolution pores, cavities, and fractures (Figure 10) (Loucks, 1999; Jiang et al., 2015, 2018; Zhu et al., 2015a).

Seepage-reflux dolostone reservoirs are formed in platform margin environments (shoal and reef facies), in which the fabric dissolution pores (also selective dissolution) are common (Figure 9B) (Jiang et al., 2016). Similarly, with the sabkha dolostone reservoirs, the pore systems (dissolution pores) of the seepage-reflux dolostones are formed by exposure to meteoric water shortly after deposition exposure caused by uplift (Figure 10). Refluxing brine could reach underlying porous formations and cause limestone to be dolomitized under shallow burial conditions (Jones and Xiao, 2005; Ngia et al., 2019). Corrosion fabrics are probably altered by late-stage regional hydrothermal activity (Jiang et al., 2016). In addition to the fabric dissolution pores, some of the intercrystalline pores form

Downloaded from http://pubs.geoscienceworld.org/aapgbull/article-pdf/105/11/2263/5431410/bltn19135.pdf
by China University of Geosciences Beijing user

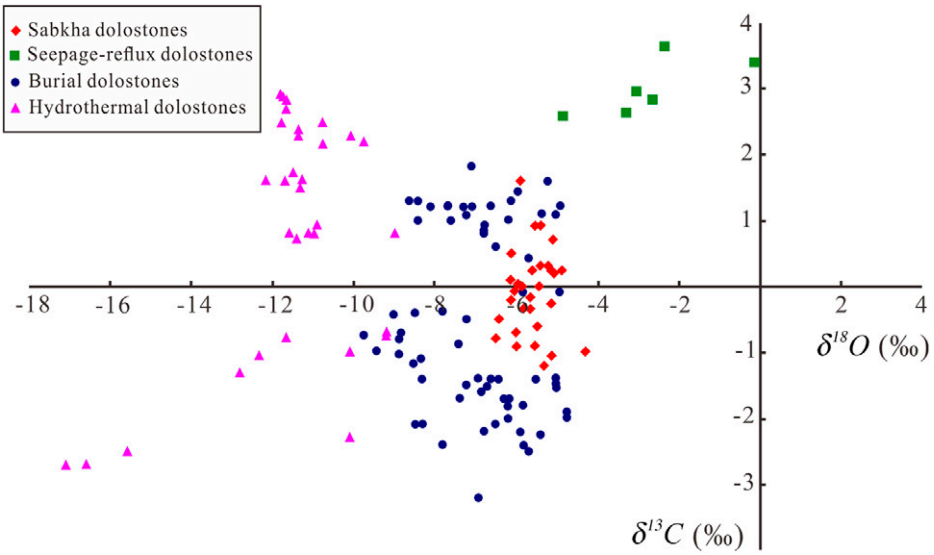

Figure 8. Scatter diagram showing the oxygen versus carbon stable isotopes for various dolostone reservoirs (Zhao et al., 2012, 2014; Zheng et al., 2013).

by seepage-reflux dolomitization, and the intercrystalline pores will be further dissolved (Figure 10).

Burial dolomitization and intense recrystallization during progressive burial result in the formation of burial dolostone reservoirs, which are characteristic of dolomites having cloudy cores but clear rims, and coarse crystalline dolomites. Intercrystalline pores and intercrystalline dissolution pores dominate burial dolostone reservoirs (Zheng et al., 2012; Zhao et al., 2014; Shen et al., 2016). Mesogenetic dissolution is another important cause of dissolution pores in burial dolostone reservoirs (Ehrenberg et al., 2012; Zhu et al., 2015a). Dissolution related to hydrocarbon generated by Cambrian source rocks and TSR could contribute to the development of intergranular dissolution (nonselective) pores (Figure 10) (Zhao et al., 2014; Zhu et al., 2015a; Jiang et al., 2016). Fabric-enlarged dissolution pores are evident because of burial dissolution (Figure 6G, H).

Hydrothermal dolostone reservoirs are mainly distributed along the faults and related fractures, allowing hydrothermal fluids to migrate upward (Figure 10) (Zhang et al., 2009; Zhu et al., 2015b). Hydrothermal-related and fracture-related vuggy dissolution pores are common (Jiang et al., 2016). These fluids migrate vertically through deep faults or fractures and will continuously dissolve dolomite minerals and form large dissolution pores (Zhu et al., 2015b). The rim of some dolomite crystals is serrated and hydrothermal minerals (fluorite) fill the pores (Figure 9D, E), indicating that the dolomite has experienced hydrothermal dissolution (Zhu et al., 2015b; Guo et al., 2016). The hydrothermal activity in the Tarim Basin is thought to be Permian and to have significantly affected the reservoir porosity in the deeply buried Cambrian dolomites (Jiang et al., 2015; Zhu et al., 2015a; Li et al., 2016).

Well-Log Response in Various Dolostone Reservoirs

Sabkha dolostone reservoirs, which contain anhydrite dissolution pores and gypsum remnants, are obvious in thin sections (Figure 11). The dark and bright spots on the images are caused by conductive anhydrite dissolution pores and resistive gypsum nodules, respectively (Lai et al., 2020) (Figure 11). Low-amplitude and straight natural GR curves (<20° API) are typical of this unit, and resistivity fluctuates greatly in sabkha dolostone reservoirs. Sonic and neutron curves show little variation, but DEN is affected by anhydrite dissolution pores (Figure 11). Sabkha dolostone reservoirs are commonly found in the northern uplift (for instance, well Yaha 10) or the Ordovician Yingshan Formation (Figure 11) (Zhao et al., 2014; Shen et al., 2016). Gypsum-bearing dolostones may have poor reservoir quality because gypsum occurs as beds or nodules,

Downloaded from http://pubs.geoscienceworld.org/aapgbull/article-pdf/105/11/2263/5431410/bltn19135.pdf
by China University of Geosciences Beijing user

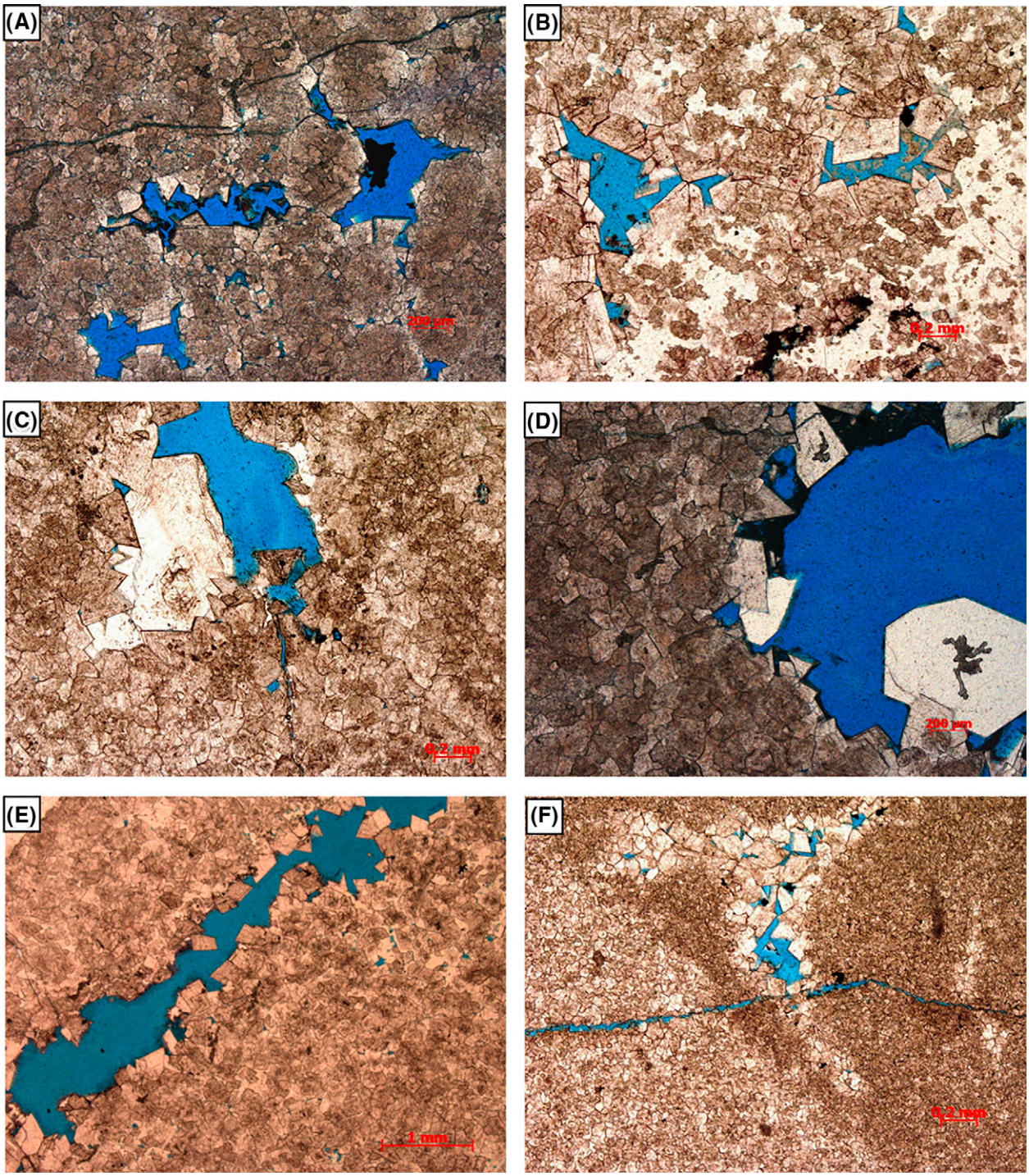

Figure 9. Characteristics of the lithology and pore systems of various porous dolostone reservoirs. (A) Fabric-obliterative dolomites and dissolution pores, well Chutan (Ct) 1, 7770.56 m, Cambrian (Є). (B) Dolomites with cloudy core and clear rims, and dissolution pores, well Zhonggu (Zg) 61 3550.42 m, Є. (C) Fluorite filling the dissolution pores, well Zg 61, 3548.6 m, Є. (D) Large dissolution pores, well Ct 1, 7769.26 m, Є. (E) Dissolution along the fracture surfaces, well Zg 582, 3603.24 m, Є. (F) Microfracture, well Zg 61, 3550.95 m, Є.

Downloaded from http://pubs.geoscienceworld.org/aapgbull/article-pdf/105/11/2263/5431410/bltn19135.pdf
by China University of Geosciences Beijing user

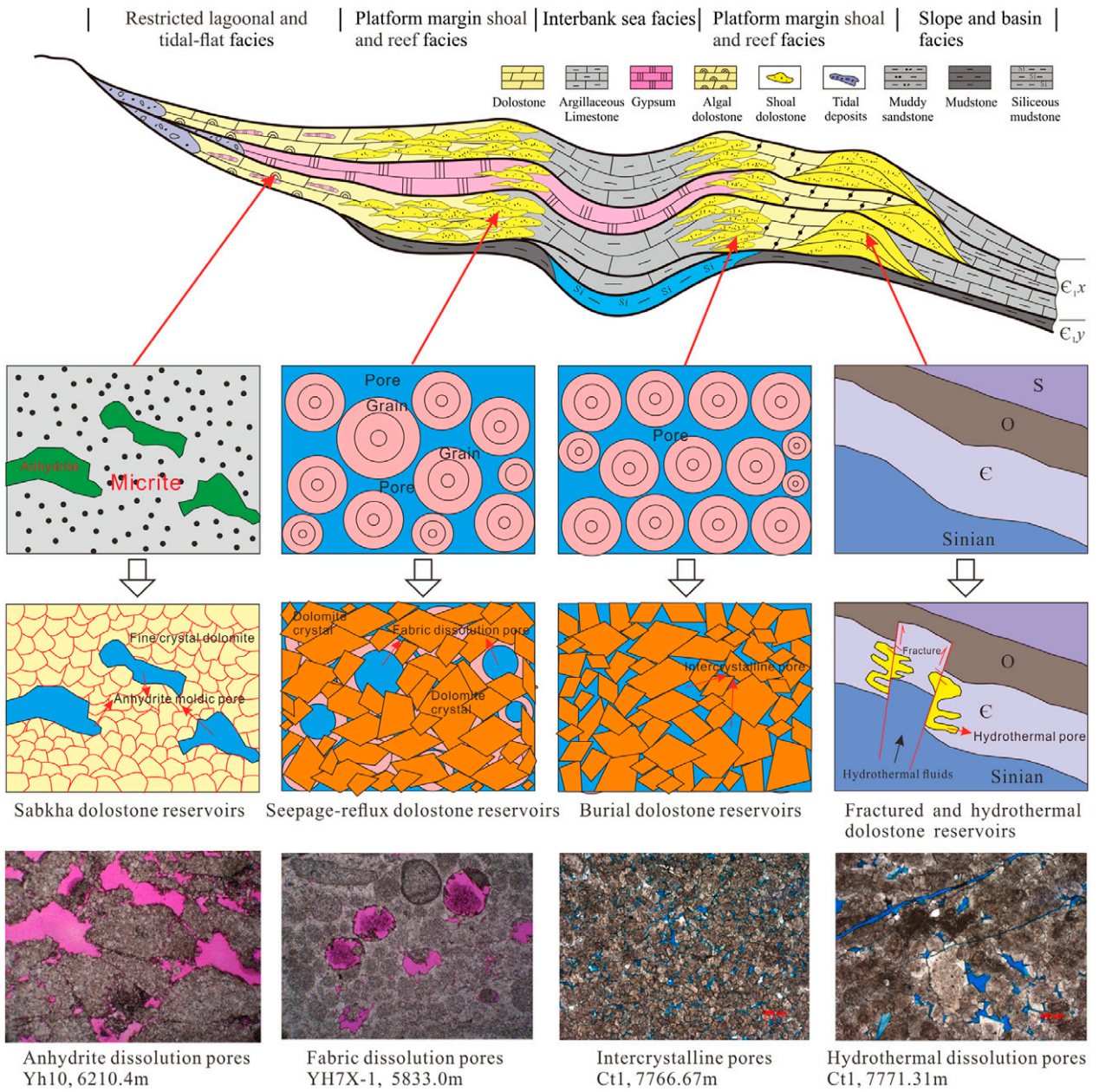

Figure 10. Genetic models of various porous dolostone reservoirs (Zheng et al., 2013, 2015; Zhao et al., 2012, 2014; Shen et al., 2016). The sedimentary facies model is based on the work of Du and Pan (2016). ϵ = Cambrian; ϵ_1x = Cambrian Xiaoerbulake Formation; ϵ_1y = Cambrian Yuertusi Formation; Ct = Chutan; O = Ordovician; S = Silurian; Si = Silica; Yh = Yaha.

and the gypsum is not dissolved (Figure 12). Thin-section analysis reveals that only minor pores are present when samples contain abundant gypsum (Figure 6C, D). The gypsum-bearing dolostone intervals are characterized by low GR, high resistivity (>200 ohm m), moderate to high photoelectric absorption cross-section index (Pe) value (>5 b/e), and high DEN (>2.9 g/cm^3) indicating low porosity (Figure 12). Additionally, white spots recognized in the image logs are caused by the high-resistivity gypsum (Figure 12).

Seepage-reflux dolostone reservoirs are associated with high-energy depositional environments. The GR curve has low amplitude (<25° API). The fabric dissolution pores, seen in thin section, are large dissolution pores or vugs, appearing as dark spots that are visible on image logs (Figure 13). The reservoir is characterized by medium-high resistivity (>100 ohm m) but low Pe

Downloaded from http://pubs.geoscienceworld.org/aapgbull/article-pdf/105/11/2263/5431410/bltn19135.pdf
by China University of Geosciences Beijing user

Downloaded from http://pubs.geoscienceworld.org/aapgbull/article-pdf/105/11/2263/5431410/bltn19135.pdf
by China University of Geosciences Beijing user

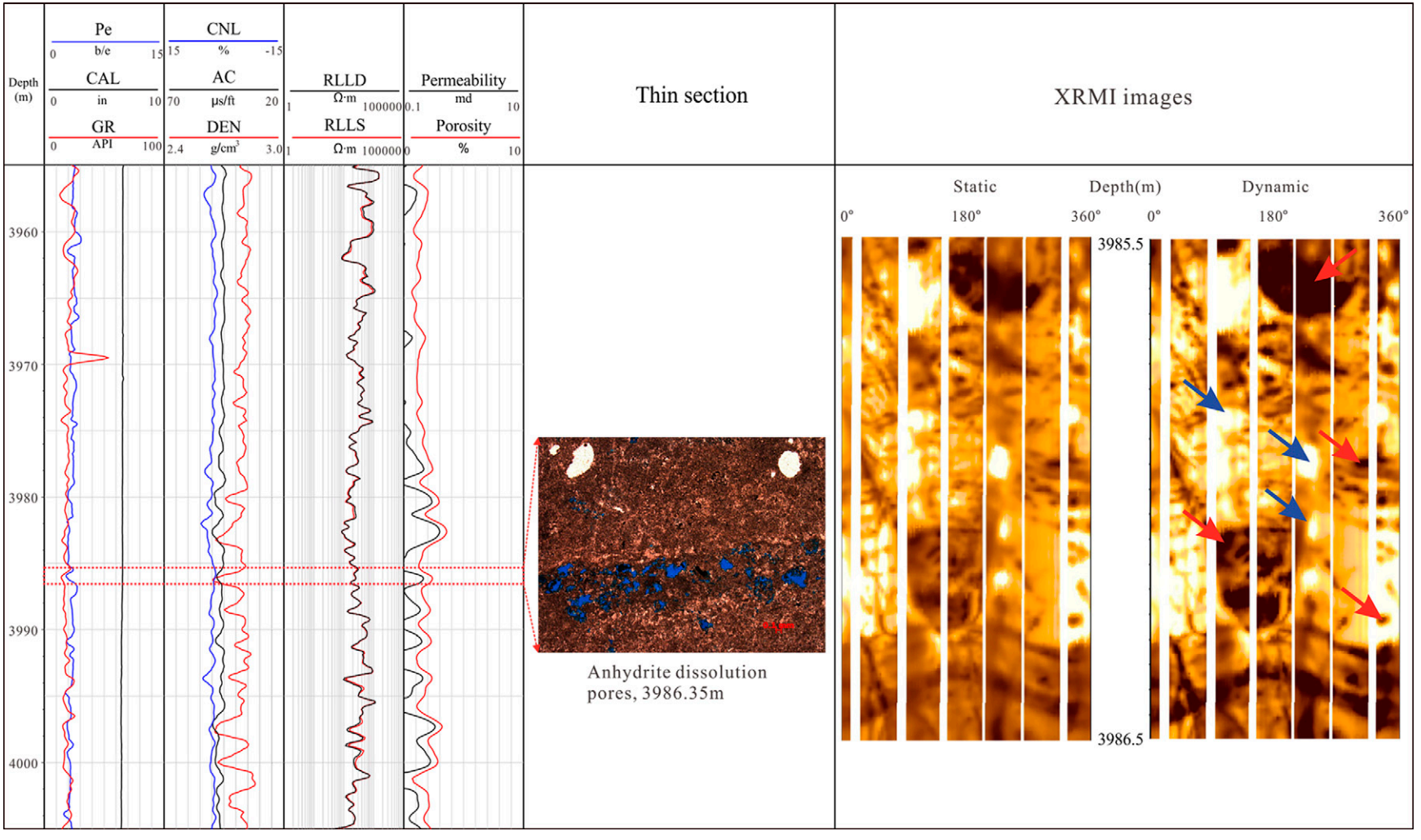

Figure 11. Well-log (conventional and image) responses and related thin sections of sabkha dolostone reservoirs (well Madong 5). The dark (red arrows) and bright spots (blue arrows) are associated with conductive anhydrite dissolution pores and resistive gypsum nodules, respectively. AC = acoustic porosity; CAL = caliper; CNL = neutron porosity; DEN = bulk density; GR = gamma ray; Pe = lithodensity; RLLD = deep resistivity; RLLS = shallow resistivity; XRMI = extended-range microimager.

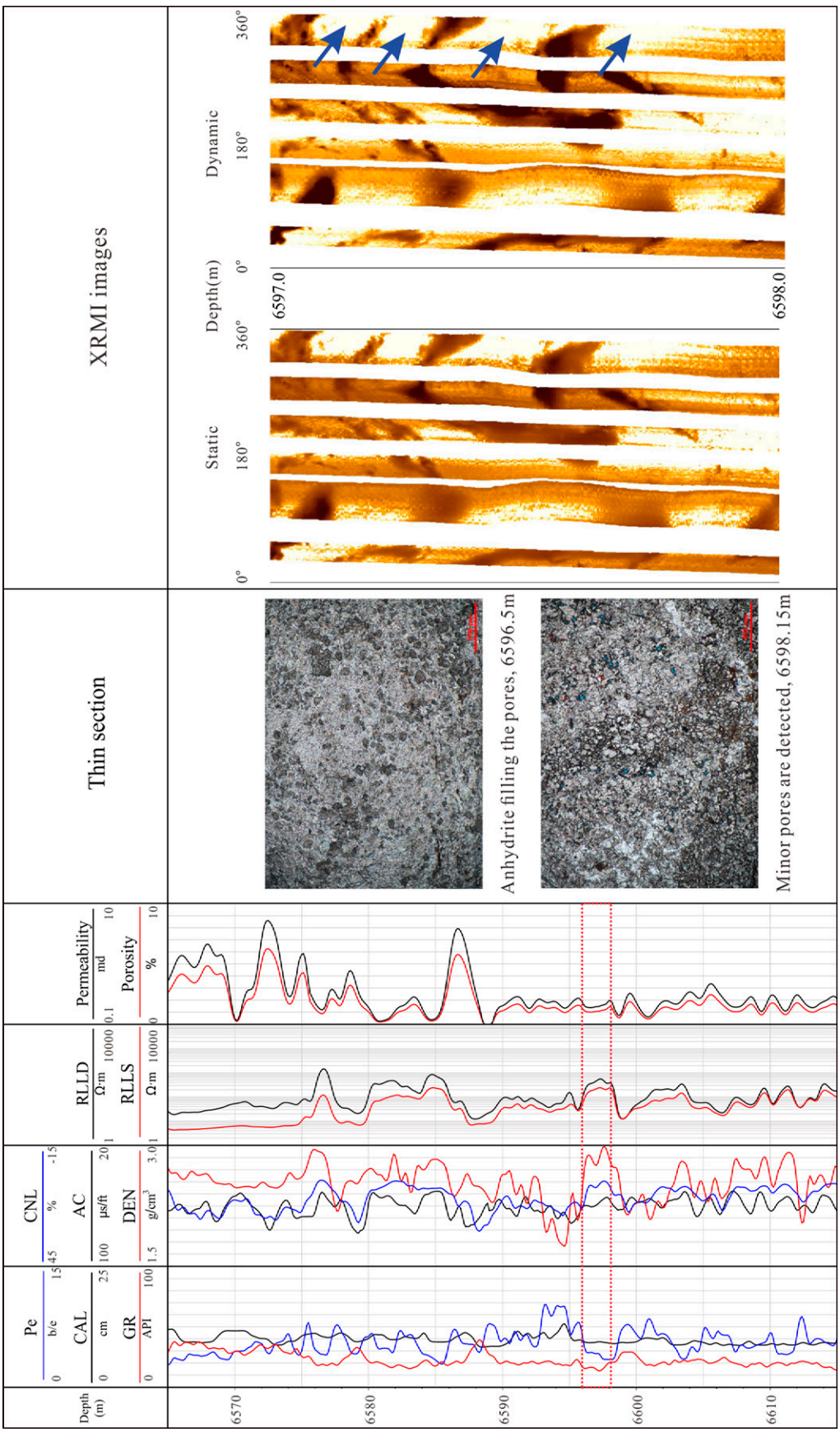

Figure 12. Well-log responses and related thin sections of gypsum-bearing dolostones (well Zhongshen 5). The white spots (blue arrows) are caused by the high-resistive gypsums. AC = acoustic porosity; CAL = caliper; CNL = neutron porosity; DEN = bulk density; GR = gamma ray; Pe = lithodensity; RLLD = deep resistivity; RLLS = shallow resistivity; XRMI = extended-range microimager.

Downloaded from http://pubs.geoscienceworld.org/aapgbull/article-pdf/105/11/2263/5431410/bltn19135.pdf
by China University of Geosciences Beijing user

Downloaded from http://pubs.geoscienceworld.org/aapgbull/article-pdf/105/11/2263/5431410/bltn19135.pdf
by China University of Geosciences Beijing user

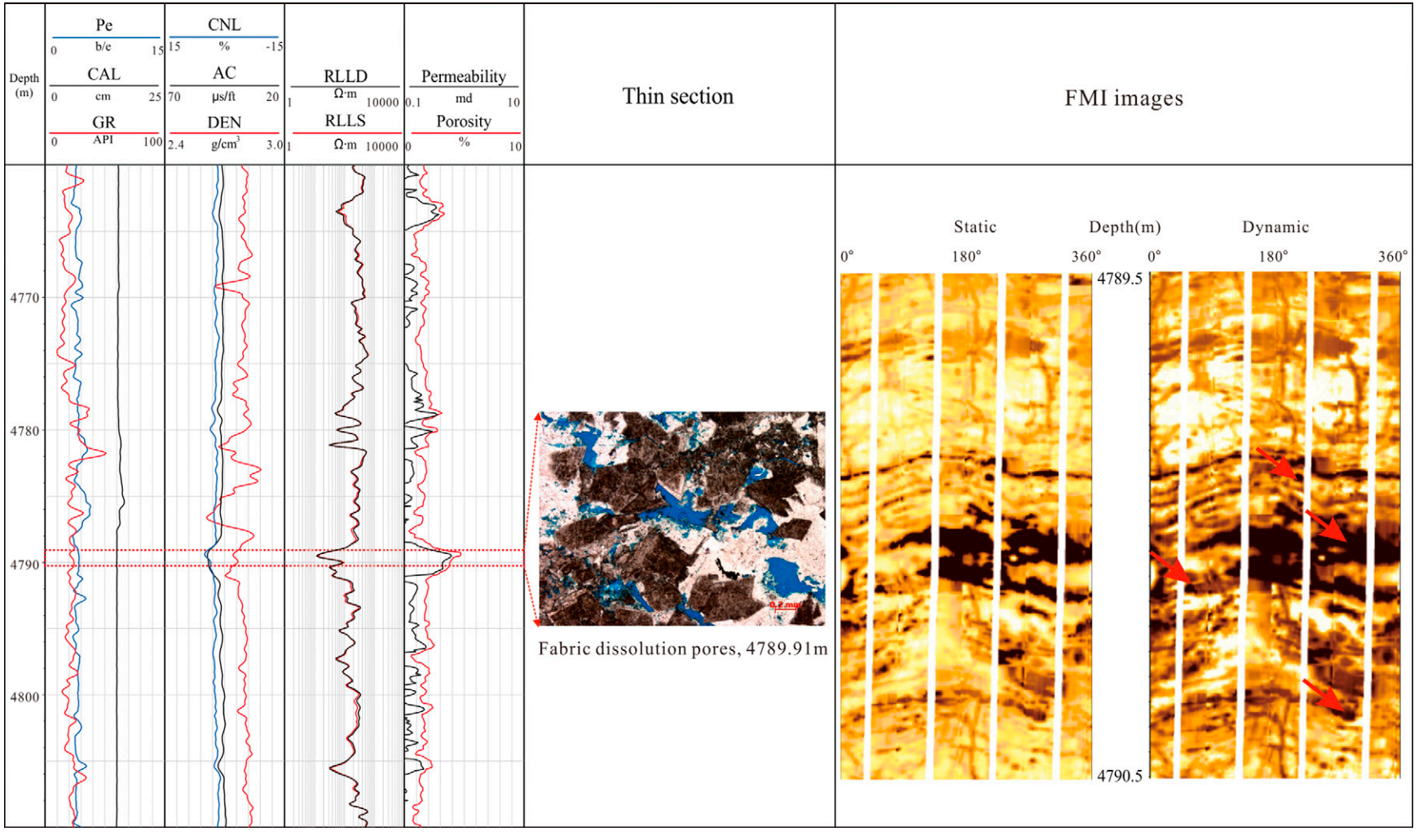

Figure 13. Well-log responses and related thin sections of seepage-reflux dolostone reservoirs (well Madong 8). The dark spots (red arrows) are caused by fabric dissolution pores. AC = acoustic porosity; CAL = caliper; CNL = neutron porosity; DEN = bulk density; FMI = fullbore formation microimager; GR = gamma ray; Pe = lithodensity; RLLD = deep resistivity; RLLS = shallow resistivity.

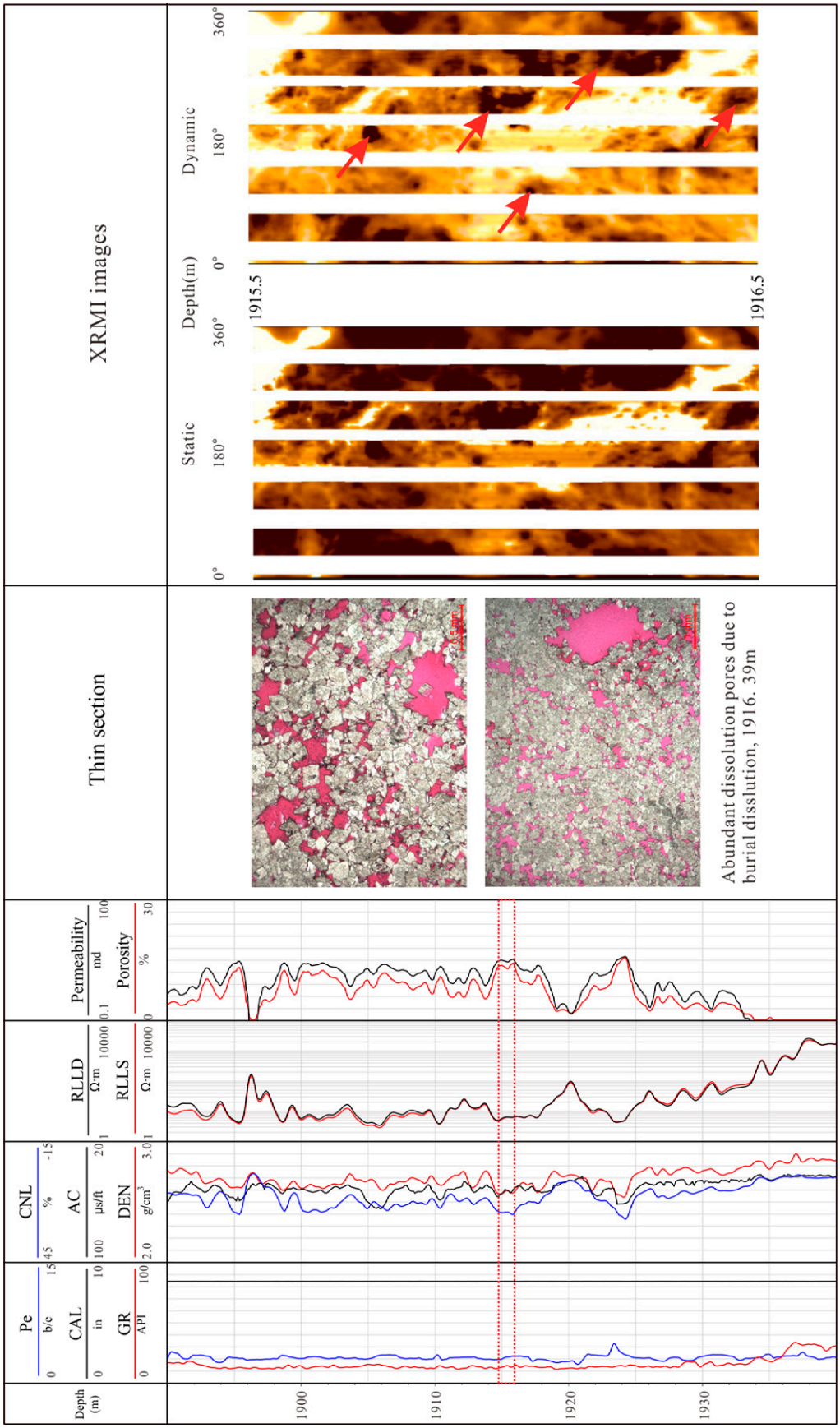

Figure 14. Well-log responses and related thin sections of burial dolostone reservoirs (well Shutan 1). The dark spots on image logs are associated with dissolution vugs. AC = acoustic porosity; CAL = caliper; CNL = neutron porosity; DEN = bulk density; GR = gamma ray; Pe = lithodensity; RLLD = deep resistivity; RLLS = shallow resistivity; XRMI = extended-range microimager.

Downloaded from http://pubs.geoscienceworld.org/aapgbull/article-pdf/105/11/2263/5431410/bltn19135.pdf
by China University of Geosciences Beijing user

Downloaded from http://pubs.geoscienceworld.org/aapgbull/article-pdf/105/11/2263/5431410/bltn19135.pdf
by China University of Geosciences Beijing user

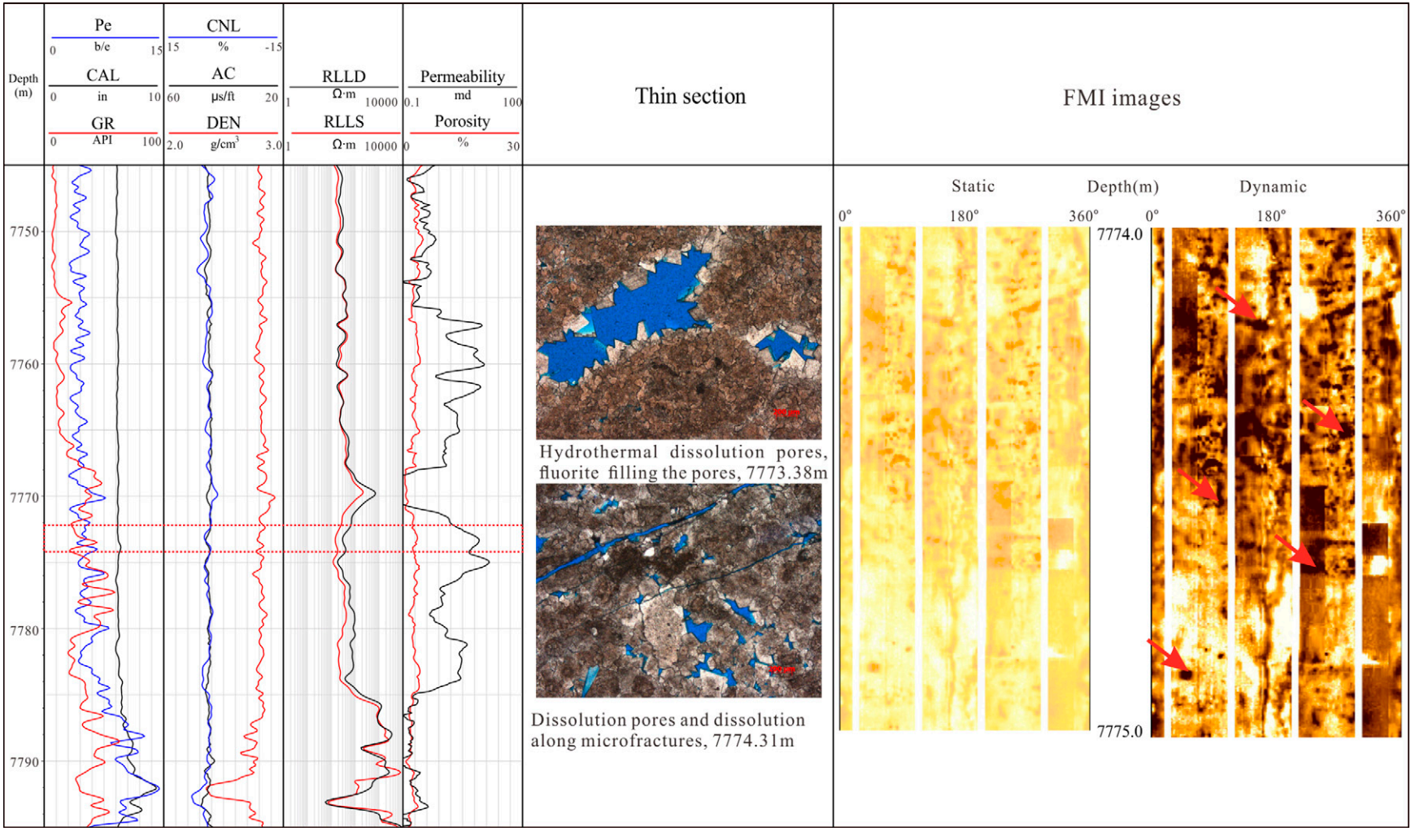

Figure 15. Well-log responses and related thin sections of hydrothermal dolostone reservoirs (well Chutan 1). AC = acoustic porosity; CAL = caliper; CNL = neutron porosity; DEN = bulk density; FMI = fullbore formation microimager; GR = gamma ray; Pe = lithodensity; RLLD = deep resistivity; RLLS = shallow resistivity.

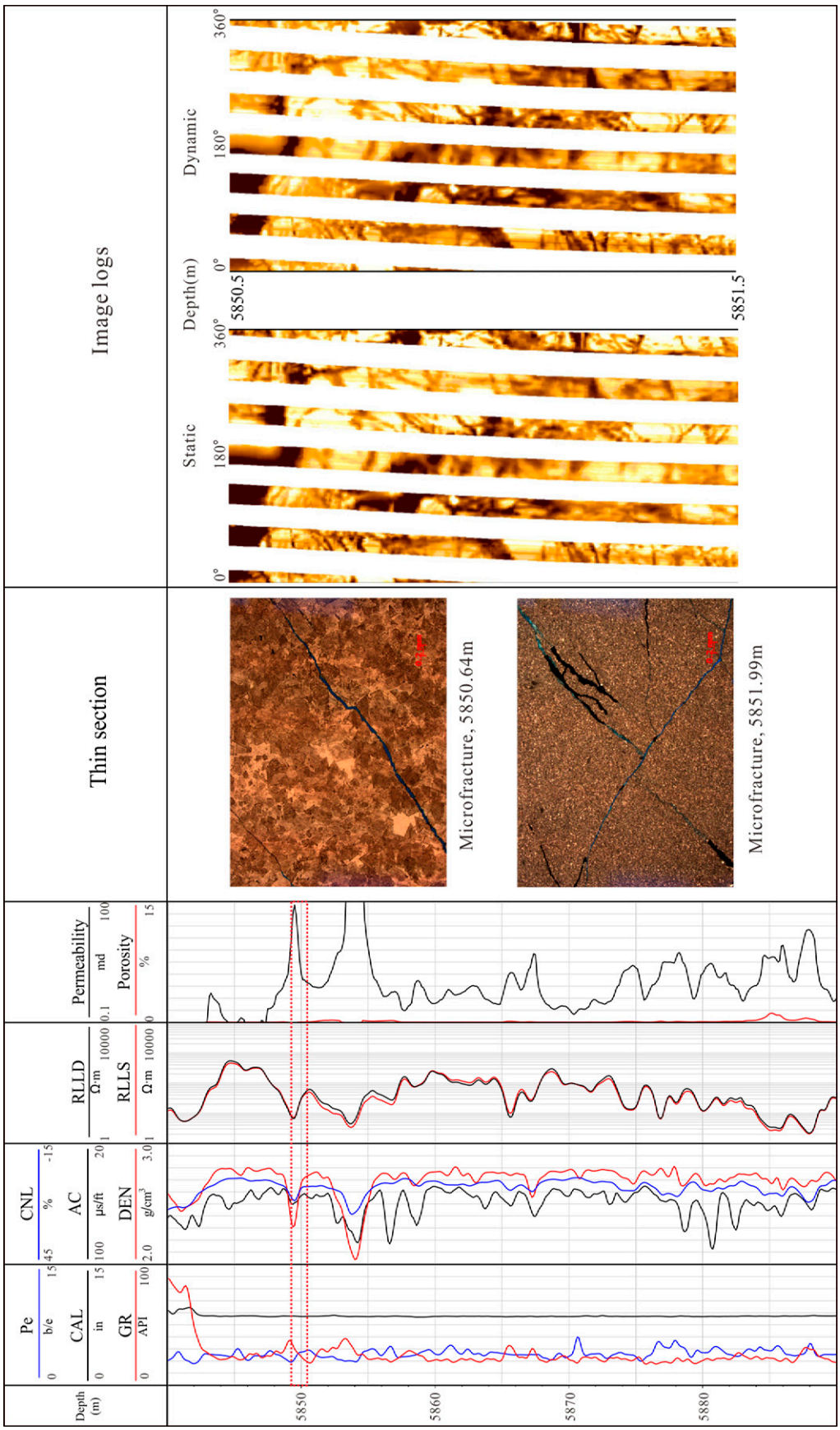

Figure 16. Well-log responses and related thin sections of fractured dolostone reservoirs (well Yaha 23-1). The presence of fractures greatly enhances permeability. AC = acoustic porosity; CAL = caliper; CNL = neutron porosity; DEN = bulk density; GR = gamma ray; Pe = lithodensity; RLLD = deep resistivity; RLLS = shallow resistivity.

Downloaded from http://pubs.geoscienceworld.org/aapgbull/article-pdf/105/11/2263/5431410/bltn19135.pdf
by China University of Geosciences Beijing user

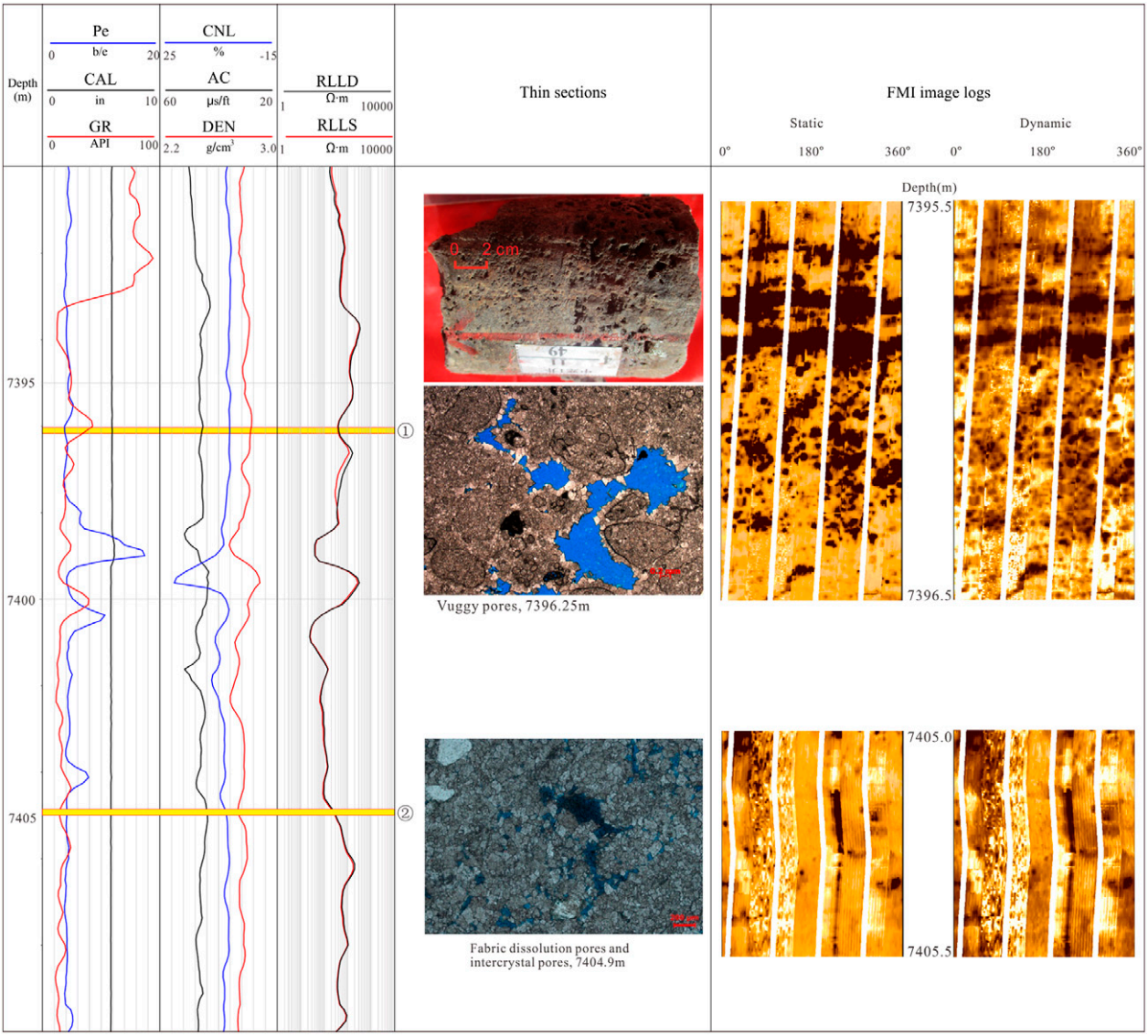

Figure 17. Calibration of predicted dolostone reservoir types with core and thin section (well Zhonghan 1). AC = acoustic porosity; CAL = caliper; CNL = neutron porosity; DEN = bulk density; FMI = fullbore formation microimager; GR = gamma ray; Pe = lithodensity; RLLD = deep resistivity; RLLS = shallow resistivity.

value (<5 b/e). Both the sonic and neutron curves are variable in seepage-reflux dolostone reservoirs, and the DEN is significantly reduced (Figure 13).

Burial (dissolution) dolostone reservoirs are characterized by intercrystalline porosity and enlarged dissolution pores (vugs) in thin section (Figure 14). Like seepage-reflux dolostone reservoirs, the burial dolostone reservoirs were deposited in high-energy depositional environments. These rocks are characterized by a low-amplitude GR curve (<15° API) and low Pe value (<5 b/e) (Figure 14). The three porosity logs (high AC values, high CNL values, but low DEN) give the signature of relatively high reservoir quality (10% porosity is high for Cambrian dolostone reservoirs in Tarim Basin). Porosity is particularly evident in the CNL log. Resistivity values are dependent on fluid properties (i.e., high resistivity if they are hydrocarbon bearing, or low resistivity if they are water bearing) (Figure 14). In addition, dark spots on image logs are associated with dissolution vugs (Lai et al., 2020) (Figure 14).

Hydrothermal dolostone reservoirs are also recognized by dissolution pores (vugs) as well as minerals such as fluorite and saddle dolomites filling the pores,

Downloaded from http://pubs.geoscienceworld.org/aapgbull/article-pdf/105/11/2263/5431410/bltn19135.pdf
by China University of Geosciences Beijing user

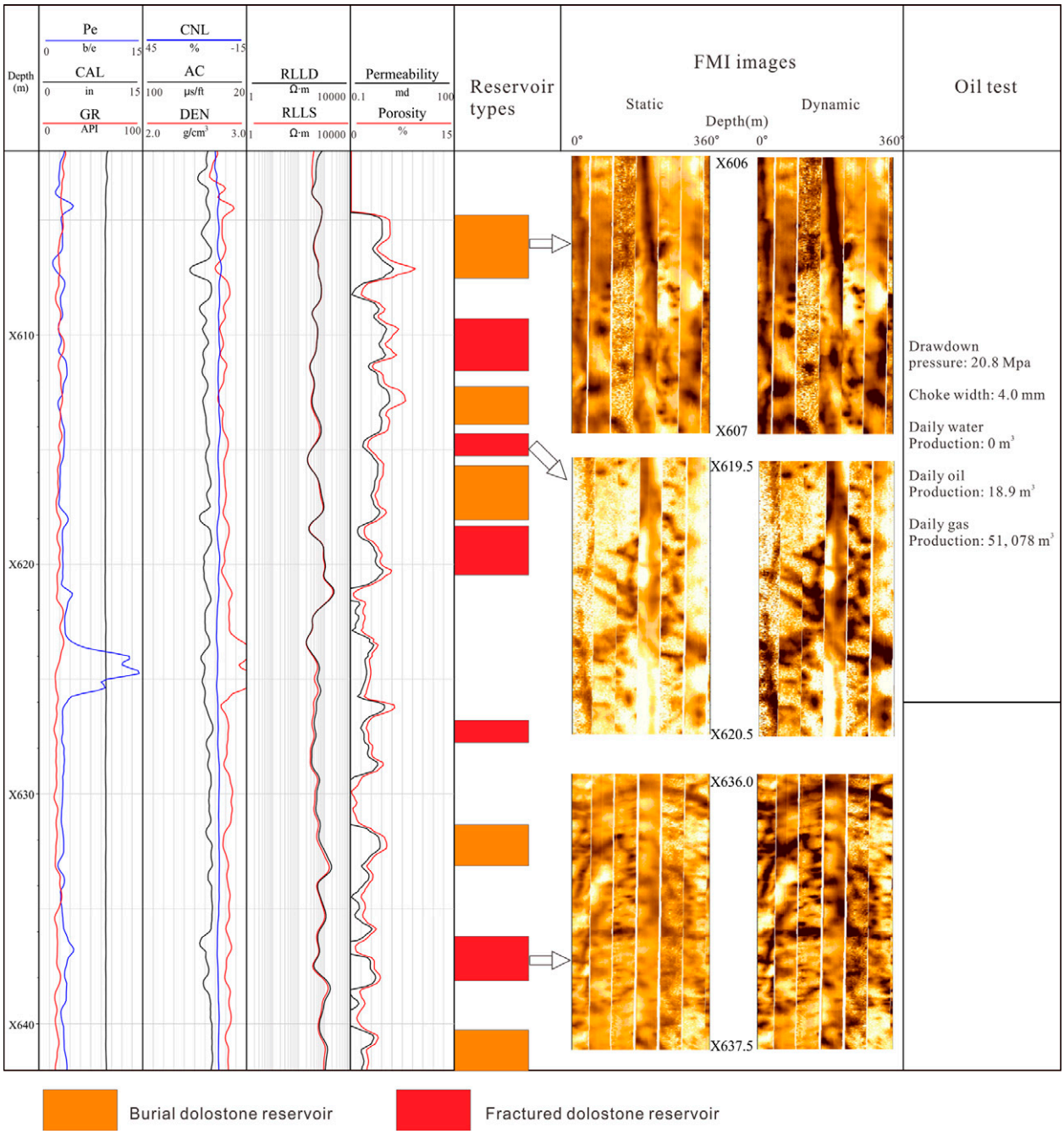

Figure 18. Prediction of dolostone reservoir types using well logs (well Zhonggu 582). AC = acoustic porosity; CAL = caliper; CNL = neutron porosity; DEN = bulk density; FMI = fullbore formation microimager; GR = gamma ray; Pe = lithodensity; RLLD = deep resistivity; RLLS = shallow resistivity.

as is similar with the burial dolostone reservoirs. Image logs exhibit dark spots (vugs) (Figure 15). Additionally, hydrothermal dolostone reservoirs are commonly associated with the fractures (conduits for hydrothermal fluid flow) (Figure 15), and the presence of fractures is an important part of enhancing dissolution (Laubach, 2003; Zeng and Li, 2009; Lai et al., 2018b). Compared with the burial dolostone reservoirs and seepage-reflux dolostone reservoirs, the hydrothermal dolostone reservoirs display distinctive GR log response (medium to high amplitude) (>30° API) caused by the presence of radioactive minerals (fluorite) (Figure 15). In addition, the sonic, neutron, and density curves indicate good reservoir quality.

Downloaded from http://pubs.geoscienceworld.org/aapgbull/article-pdf/105/11/2263/5431410/bltn19135.pdf
by China University of Geosciences Beijing user

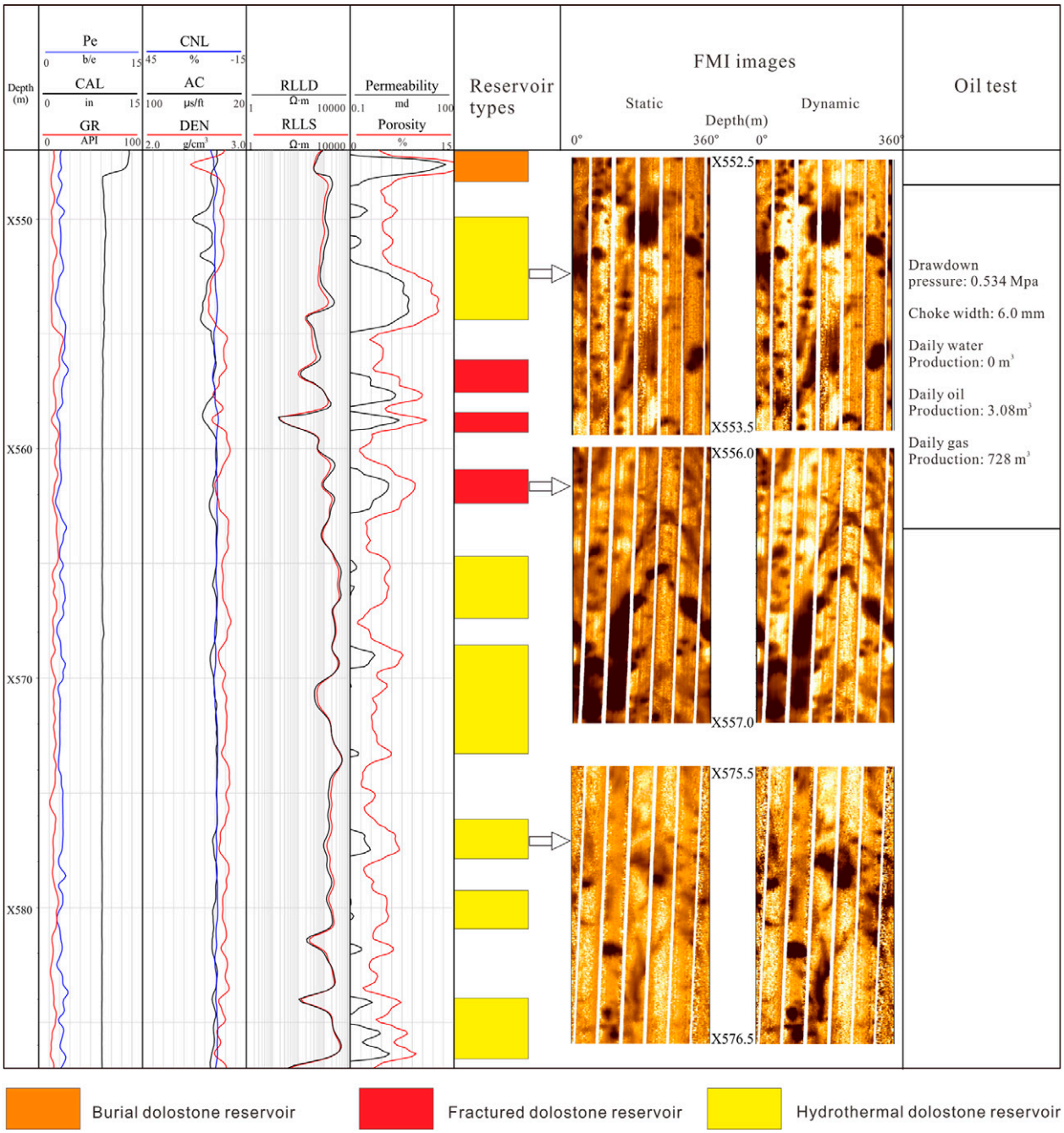

Figure 19. Prediction of dolostone reservoir types using well logs (well Zhonggu 61). Note that high permeability can be encountered in low-porosity layers because of the presence of fractures. AC = acoustic porosity; CAL = caliper; CNL = neutron porosity; DEN = bulk density; FMI = fullbore formation microimager; GR = gamma ray; Pe = lithodensity; RLLD = deep resistivity; RLLS = shallow resistivity.

Resistivity values are generally low (<100 ohm m) (Figure 15) unless the pores are hydrocarbon saturated.

Fractures are easily recognized in the conventional well logs as well as image logs (Khoshbakht et al., 2012; Lai et al., 2017b, 2018a, b; Lyu et al., 2016). Rapid decrease in the resistivity, increase in the AC traveltime, and a decrease in DEN are all characteristics of fractures (Khoshbakht et al., 2009; Zeng, 2010; Aghli et al., 2016; Lai et al., 2017b; Nian et al., 2017). In addition, the fractures are recognized as sine waves (conductive fractures appearing as dark sinusoidal waves) on image logs

Downloaded from http://pubs.geoscienceworld.org/aapgbull/article-pdf/105/11/2263/5431410/bltn19135.pdf
by China University of Geosciences Beijing user

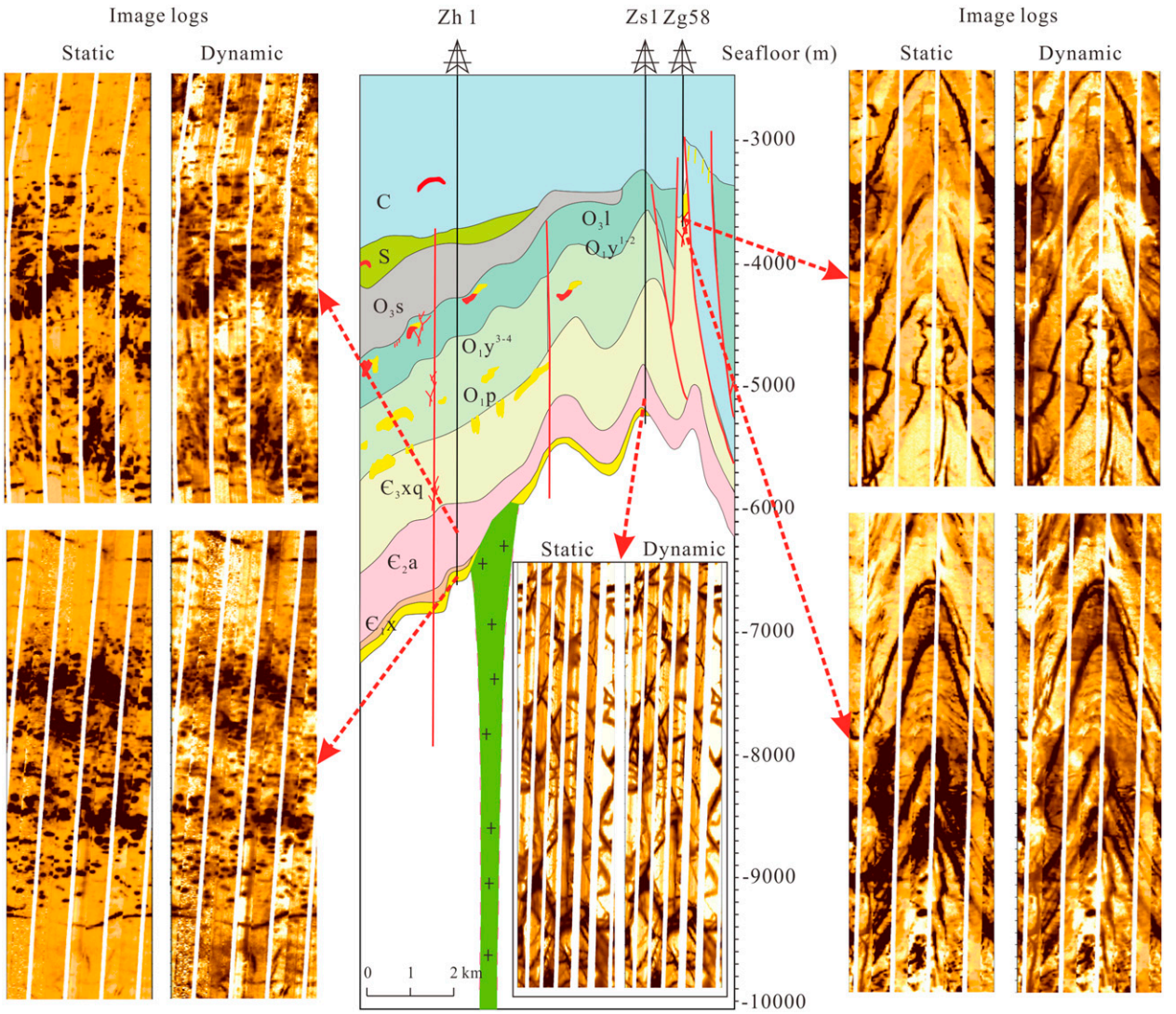

Figure 20. Cross section of the well Zhonghan (Zh) 1-Zhongshen (Zg) 5 and related image logs. The cross-section map is based on the work of petroleum exploration and development of PetroChina Tarim Oilfield Company. Each image log stands for 2 m thick. ϵ_1x = Cambrian Xiaoerbulake Formation; ϵ_2a = Cambrian Awatage Formation; ϵ_3xq = Cambrian Xiaqiulitage Formation; C = Cambrian; O_1y^{3-4} = third and fourth members of Ordovician Yingshan Formation; O_3l = Ordovician Lianglitage Formation; O_3s = Ordovician Sangtamu Formation; O_1p = Ordovician Penglaiba Formation; O_1y^{1-2} = first and second members of Ordovician Yingshan Formation; S = Silurian.

(Kosari et al., 2015; Wilson et al., 2015; Lai et al., 2018b) (Figure 16).

Well-Log Prediction of Dolostone Reservoirs

Table 1 lists the characteristics of the four types of dolostone reservoirs (Figures 11–16).

The well Zh 1 is chosen to test the established predictable model, and the predictable results are calibrated with the core and thin-section data (Figure 17). Layer 1 (marked as 1) in Figure 17 is characterized by low-medium GR, medium CNL values, but low DEN, and the dark spots on the image logs suggest vugs, so all logs suggest the presence of burial dolostone reservoirs. Vugs are documented by core and thin-section study, which is typical of burial dolostone reservoirs (Figure 17). In addition, layer 2 (marked as 2), which is characterized by low GR, low DEN, high CNL, and medium-high resistivity, is a typical

Downloaded from http://pubs.geoscienceworld.org/aapgbull/article-pdf/105/11/2263/5431410/bltn19135.pdf
by China University of Geosciences Beijing user

seepage-reflux dolostone reservoir and has minor dark spots. When calibrated with the thin sections, it is confirmed that only fabric dissolution pores are presented, indicating that the layer 2 is a typical seepage-reflux dolostone reservoir (Figure 17).

The following discussion demonstrates how the distribution of porous dolostone reservoirs in wells Zg 582 and Zg 61 can be recognized by comprehensive analysis of conventional well logs (GR, three porosity logs, and resistivity log) and image logs. Vugs in the well Zg 582 are evident in cores and thin sections, and two types of dolostone reservoirs (burial dolostone reservoirs and fractures) are present. The porous dolostone is plotted with conventional well and image logs (Figure 18). Burial dolostone reservoirs are present as dark spots on the image logs. The GR curve has low variability and is straight. The three porosity logs show the favorable reservoir quality in the porous intervals, and the medium to high-resistivity logs suggest hydrocarbons are present (Figure 18). Fractured dolostone intervals are recognized by rapidly decreasing resistivity and increasing AC transit time. Dark sinusoidal waves on the image logs indicate the presence of fractures. Dark spots are observed along the fracture surface on the image logs, indicating dissolution along the fracture plane, further enhancing reservoir quality (Figure 18). In the interval X599.0 to X626.0 m, there are six intervals in which the dolostone reservoirs exist. These intervals flowed hydrocarbons at the rate of 18.9 m^3/day (118.9 BOPD) and natural gas at the rate of 51,078 m^3/day (1800 MCFGD).

Intercrystalline pores and dissolution-enlarged pores (vugs on core observation) (Figure 6E, F) were identified in thin sections in well Zg 61. Hydrothermal fluorite (Figure 9C) is present in the pores. Analysis of well logs identifies three types of dolostone reservoirs (Figure 19). The first is burial dolostone reservoir, in which the pore systems are dominantly intercrystalline (dissolution) pores. The burial dolostone reservoir is distributed in the top intervals of Zg 61, and well-log responses in these zones are similar to the burial dolostone reservoir in Figure 18. The second is hydrothermal dolostone reservoir, which has both large dissolution pores and fracture-enlarged pores (Figures 6J; 6C, D) that show up as large dark spots on the image logs, and the three porosity logs have higher porosity values (Figure 19). The degree of dissolution along fracture planes is also high, resulting in the development of fractured hydrothermal dolostone reservoirs (Luczaj et al., 2006). Four dolostone reservoir intervals are recognized in the interval from X550.0 to X565.0 m. These zones flowed oil at the rate of 3.08 m^3/day (19 BOPD) and natural gas production of 728 m^3/day (25.7 MCFGD) (drawdown pressure: 0.534 MPa [77.45 psi]; choke width: 6 mm). The intervals, in which no "reservoir types" are divided in Figures 18 and 19, are tight dolostone with little or no porosity.

The cross section Zh 1-Zs 5-Zg 58 (interpreted from seismic profile) reveals that the wells Zg 58 and Zs 5 are drilled in the faulted zones, and the dolostones are highly fractured, forming fractured dolostone reservoirs. The image logs confirm that the fractures are abundant in wells Zg 58 and Zs 5; conversely, dark spots, or vugs, are much less common (Figure 20).

Well Zh 1 had not been drilled into the faulted zones. However, igneous rocks and related hydrothermal fluids intruded into the surrounding rocks. Therefore, the dolostones contain abundant vugs and fabric-enlarged dissolution pores, which are commonly detected by core and thin sections (Figure 17), and they are also evident in the image logs (Figure 20). Therefore, the dolostone types in well Zh 1 are mainly burial dolostones and hydrothermal dolostones, but there are no evident fractures encountered (Figure 20).

CONCLUSIONS

Six types of dolomite are recognized in terms of crystal size and presence of residual grains, including D1, D2, D3 (oolites, intraclasts), D4, Cd, and Sd. Four types of porous dolostone reservoirs are recognized in the Cambrian dolostones of Tarim Basin identified by thin section, CL analysis, and isotopic composition. These are sabkha dolostones, seepage-reflux dolostones, burial dolostones, and hydrothermal dolostones. The pore systems include anhydrite dissolution pores, intercrystalline pores, intercrystalline dissolution pores, fabric dissolution pores, and microfractures.

Understanding the dolomitization process through depositional facies analysis, sequence stratigraphy, burial dissolution, hydrothermal geofluids, and tectonic evolution builds a geological genetic model of the four dolostone reservoirs and fractures. The various dolomite reservoir types can be recognized in

Downloaded from http://pubs.geoscienceworld.org/aapgbull/article-pdf/105/11/2263/5431410/bltn19135.pdf
by China University of Geosciences Beijing user

well logs by calibrating image logs and conventional well logs with core study and thin sections. The distribution of porous dolostone reservoir types and fractured dolostone reservoirs in wells of the Tarim Basin is confirmed by high hydrocarbon flow rates in the wells.

REFERENCES CITED

Aghli, G., R. Moussavi-Harami, and R. Mohammadian, 2020, Reservoir heterogeneity and fracture parameter determination using electrical image logs and petrophysical data (a case study, carbonate Asmari Formation, Zagros Basin, SW Iran): Petroleum Science, v. 17, no. 1, p. 51–69, doi:10.1007/s12182-019-00413-0.

Aghli, G., B. Soleimani, R. Moussavi-Harami, and R. Mohammadian, 2016, Fractured zones detection using conventional petrophysical logs by differentiation method and its correlation with image logs: Journal of Petroleum Science Engineering, v. 142, p. 152–162, doi:10.1016/j.petrol.2016.02.002.

Al-Aasm, I., J. Lonnee, and J. Clarke, 2002, Multiple fluid flow event and the formation of saddle dolomite: Case studies from Middle Devonian of the Western Canada Sedimentary Basin: Marine and Petroleum Geology, v. 19, no. 3, p. 209–217, doi:10.1016/S0264-8172(02)00013-2.

Aschwanden, L., L. W. Diamond, and A. Adams, 2019, Effects of progressive burial on matrix porosity and permeability of dolostones in the foreland basin of the Alpine Orogen, Switzerland: Marine and Petroleum Geology, v. 100, p. 148–164, doi:10.1016/j.marpetgeo.2018.10.055.

Bai, X., S. Zhang, Q. Huang, X. Ding, and S. Zhang, 2016, Origin of dolomite in the Middle Ordovician peritidal platform carbonates in the northern Ordos Basin, western China: Petroleum Science, v. 13, no. 3, p. 434–449, doi:10.1007/s12182-016-0114-5.

Brekke, H., J. A. MacEachern, T. Roenitz, and S. E. Dashtgard, 2017, The use of microresistivity image logs for facies interpretations: An example in point-bar deposits of the McMurray Formation, Alberta, Canada: AAPG Bulletin, v. 101, no. 5, p. 655–682, doi:10.1306/08241616014.

Cai, C. F., W. Hu, and R. H. Worden, 2001, Thermochemical sulphate reduction in Cambro-Ordovician carbonate in Central Tarim: Marine and Petroleum Geology, v. 18, no. 6, p. 729–741, doi:10.1016/S0264-8172(01)00028-9.

Cai, C. F., C. M. Zhang, R. H. Worden, T. K. Wang, H. X. Li, L. Jiang, S. Y. Huang, and B. S. Zhang, 2015, Application of sulfur and carbon isotopes to oil–source rock correlation: A case study from the Tazhong area, Tarim Basin, China: Organic Geochemistry, v. 83–84, p. 140–152, doi:10.1016/j.orggeochem.2015.03.012.

Chen, J., Y. Xu, and D. Huang, 2000, Geochemical characteristics and origin of natural gas in Tarim Basin, China: AAPG Bulletin, v. 84, no. 5, p. 591–606.

Dong, S., D. Chen, H. Qing, X. Zhou, D. Wang, Z. Guo, M. Jiang, and Y. Qian, 2013, Hydrothermal alteration of dolostones in the Lower Ordovician, Tarim Basin, NW China: Multiple constraints from petrology, isotope geochemistry and fluid inclusion microthermometry: Marine and Petroleum Geology, v. 46, p. 270–286, doi:10.1016/j.marpetgeo.2013.06.013.

Du, J., and W. Pan, 2016, Accumulation conditions and play targets of oil and gas in the Cambrian subsalt dolomite, Tarim Basin, NW China: Petroleum Exploration and Development, v. 43, no. 3, p. 360–374, doi:10.1016/S1876-3804(16)30043-X.

Du, Y., T. Fan, H. G. Machel, and Z. Gao, 2018, Genesis of Upper Cambrian-Lower Ordovician dolomites in the Tahe oilfield, Tarim basin, NW China: Several limitations from petrology, geochemistry, and fluid inclusions: Marine and Petroleum Geology, v. 91, p. 43–70, doi:10.1016/j.marpetgeo.2017.12.023.

Ehrenberg, S. N., G. P. Eberli, M. Keramati, and S. A. Moallemi, 2006, Porosity-permeability relationships in interlayered limestone-dolostone reservoirs: AAPG Bulletin, v. 90, no. 1, p. 91–114, doi:10.1306/08100505087.

Ehrenberg, S. N., O. Walderhaug, and K. Bjørlykke, 2012, Carbonate porosity creation by mesogenetic dissolution: Reality or illusion?: AAPG Bulletin, v. 96, no. 2, p. 217–233, doi:10.1306/05031110187.

El Sharawy, M. S., and B. S. Nabawy, 2016, Geological and petrophysical characterization of the Lower Senonian Matulla Formation in southern and central Gulf of Suez, Egypt: Arabian Journal for Science and Engineering, v. 41, no. 1, p. 281–300, doi:10.1007/s13369-015-1806-7.

Folkestad, A., Z. Veselovsky, and P. Roberts, 2012, Utilising borehole image logs to interpret delta to estuarine system: A case study of the subsurface Lower Jurassic Cook Formation in the Norwegian northern North Sea: Marine and Petroleum Geology, v. 29, no. 1, p. 255–275, doi:10.1016/j.marpetgeo.2011.07.008.

Fu, Q., 2019, Characterization and discrimination of paleokarst breccias and pseudobreccias in carbonate rocks: Insight from Ordovician strata in the northern Tarim Basin, China: Sedimentary Geology, v. 382, p. 61–74, doi:10.1016/j.sedgeo.2019.01.007.

Gao, Z., Q. Ding, and X. Hu, 2015, Characteristics and controlling factors of carbonate intra-platform shoals in the Tarim Basin, NW China: Journal of Petroleum Science Engineering, v. 127, p. 20–34, doi:10.1016/j.petrol.2015.01.027.

Gao, Z., and T. Fan, 2015, Carbonate platform-margin architecture and its influence on Cambrian-Ordovician reef-shoal development, Tarim Basin, NW China: Marine and Petroleum Geology, v. 68, p. 291–306, doi:10.1016/j.marpetgeo.2015.08.033.

Gao, Z., Z. Liu, S. Gao, Q. Ding, S. Wu, and S. Liu, 2016, Characteristics and genetic models of Lower Ordovician carbonate reservoirs in southwest Tarim Basin, NW China: Journal of Petroleum Science Engineering, v. 144, p. 99–112, doi:10.1016/j.petrol.2016.03.007.

Guo, C., D. Chen, H. Qing, S. Dong, G. Li, D. Wang, Y. Qian, and C. Liu, 2016, Multiple dolomitization and later hydrothermal alteration on the Upper Cambrian-Lower Ordovician carbonates in the northern Tarim Basin, China: Marine and Petroleum Geology, v. 72, p. 295–316, doi:10.1016/j.marpetgeo.2016.01.023.

Downloaded from http://pubs.geoscienceworld.org/aapgbull/article-pdf/105/11/2263/5431410/bltn19135.pdf
by China University of Geosciences Beijing user

Guo, C., D. Chen, Y. Song, X. Zhou, Y. Ding, and G. Zhang, 2018, Depositional environments and cyclicity of the early Ordovician carbonate ramp in the western Tarim basin (NW China): Journal of Asian Earth Sciences, v. 158, p. 29–48, doi:10.1016/j.jseaes.2018.02.006.

Haas, J., T. Budai, O. Győri, and S. Kele, 2014, Multiphase partial and selective dolomitization of Carnian reef limestone (Transdanubian Range, Hungary): Sedimentology, v. 61, no. 3, p. 836–859, doi:10.1111/sed.12088.

He, Z., X. Jin, Y. Wo, H. Li, Z. Bai, C. Jiao, and Z. Zhang, 2016, Hydrocarbon accumulation characteristics and exploration domains of ultra-deep marine carbonates in China: Zhongguo Shiyou Kantan, v. 21, no. 1, p. 3–14.

Hu, W., J. Zhu, X. Wang, X. You, and K. He, 2014, Characteristics, origin and geological implications of the Cambrian microbial dolomite in Keping area, Tarim Basin [in Chinese with English abstract]: Oil & Gas Geology, v. 35, no. 6, p. 860–869.

Hu, Z., W. Hu, C. Liu, F. Sun, Y. Liu, and W. Li, 2019, Conservative behavior of Mg isotopes in massive dolostones: From diagenesis to hydrothermal reworking: Sedimentary Geology, v. 381, p. 65–75, doi:10.1016/j.sedgeo.2018.12.007.

Huang, Q.-Y., S.-N. Zhang, S.-Y. Zhang, D. Liu, and N. Ye, 2014, Textural control on the development of dolomite reservoir: A study from the Cambrian-Ordovician dolomite, central Tarim Basin, NW China [in Chinese with English abstract]: Natural Gas Geoscience, v. 25, no. 3, p. 341–350, 470.

Iapponi, F., T. Bechstadt, M. Boni, D. A. Banks, and J. Schneider, 2014, Hydrothermal dolomitization in a complex geodynamic setting (Lower Palaeozoic, northern Spain): Sedimentology, v. 61, no. 2, p. 411–443, doi:10.1111/sed.12060.

Jafari, J., A. Mahboubi, R. Moussavi-Harami, and I. S. Al-Aasm, 2020, The effects of diagenesis on the petrophysical and geochemical attributes of the Asmari Formation, Marun oil field, southwest Iran: Petroleum Science, v. 17, no. 2, p. 292–316, doi:10.1007/s12182-019-00421-0.

Jiang, L., C. Cai, R. H. Worden, S. F. Crowley, L. Jia, K. Zhang, and I. J. Duncan, 2016, Multiphase dolomitization of deeply buried Cambrian petroleum reservoirs, Tarim Basin, north-west China: Sedimentology, v. 63, no. 7, p. 2130–2157, doi:10.1111/sed.12300.

Jiang, L., W. Pan, C. Cai, L. Jia, L. Pan, T. Wang, H. Li, S. Chen, and Y. Chen, 2015, Fluid mixing induced by hydrothermal activity in the Ordovician carbonates in Tarim Basin, China: Geofluids, v. 15, no. 3, p. 483–498, doi:10.1111/gfl.12125.

Jiang, L., R. H. Worden, and C. Cai, 2014, Thermochemical sulfate reduction and fluid evolution of the Lower Triassic Feixianguan Formation sour gas reservoirs, northeast Sichuan Basin, China: AAPG Bulletin, v. 98, no. 5, p. 947–973, doi:10.1306/10171312220.

Jiang, L., R. H. Worden, C. F. Cai, A. Shen, and S. F. Crowley, 2018, Diagenesis of an evaporite-related carbonate reservoir in deeply buried Cambrian strata, Tarim basin, Northwest China: AAPG Bulletin, v. 102, no. 1, p. 77–102, doi:10.1306/0328171608517048.

Jin, Z., D. Zhu, W. Hu, X. Zhang, J. Zhang, and Y. Song, 2009, Mesogenetic dissolution of the middle Ordovician limestone in the Tahe oilfield of Tarim basin, NW China: Marine and Petroleum Geology, v. 26, no. 6, p. 753–763, doi:10.1016/j.marpetgeo.2008.08.005.

Jones, G. D., and Y. Xiao, 2005, Dolomitization, anhydrite cementation, and porosity evolution in a reflux system: Insights from reactive transport models: AAPG Bulletin, v. 89, no. 5, p. 577–601, doi:10.1306/12010404078.

Khoshbakht, F., M. Azizzadeh, H. Memarian, G. H. Nourozi, and S. A. Moallemi, 2012, Comparison of electrical image log with core in a fractured carbonate reservoir: Journal of Petroleum Science Engineering, v. 86–87, p. 289–296, doi:10.1016/j.petrol.2012.03.007.

Khoshbakht, F., H. Memarian, and M. Mohammadnia, 2009, Comparison of Asmari, Pabdeh and Gurpi formation's fractures, derived from image log: Journal of Petroleum Science Engineering, v. 67, no. 1–2, p. 65–74, doi:10.1016/j.petrol.2009.02.011.

Kosari, E., S. Ghareh-Cheloo, A. Kadkhodaie-Ilkhchi, and A. Bahroudi, 2015, Fracture characterization by fusion of geophysical and geomechanical data: A case study from the Asmari reservoir, the Central Zagros fold-thrust belt: Journal of Geophysics and Engineering, v. 12, no. 1, p. 130–143, doi:10.1088/1742-2132/12/1/130.

Lai, J., K. Chen, Y. Xin, X. Wu, X. Chen, K. Yang, Q. Song, G. Wang, X. Ding, 2021, Fracture characterization and detection in the deep Cambrian dolostones in the Tarim Basin, China: Insights from borehole image and sonic logs: Journal of Petroleum Science and Engineering, v.196, 107659.

Lai, J., X. Pang, Q. Xiao, Y. Shi, H. Zhang, T. Zhao, J. Chen, G. Wang, and Z. Qin, 2019a, Prediction of reservoir quality in carbonates via porosity spectrum from image logs: Journal of Petroleum Science Engineering, v. 173, p. 197–208, doi:10.1016/j.petrol.2018.10.022.

Lai, J., G. Wang, Y. Chai, Y. Xin, Q. Wu, X. Zhang, and Y. Sun, 2017a, Deep burial diagenesis and reservoir quality evolution of high-temperature, high-pressure sandstones: Examples from Lower Cretaceous Bashijiqike Formation in Keshen area, Kuqa depression, Tarim basin of China: AAPG Bulletin, v. 101, no. 6, p. 829–862, doi:10.1306/08231614008.

Lai, J., G. Wang, Z. Fan, Z. Wang, J. Chen, Z. Zhou, S. Wang, and C. Xiao, 2017b, Fracture detection in oil-based drilling mud using a combination of borehole image and sonic logs: Marine and Petroleum Geology, v. 84, p. 195–214, doi:10.1016/j.marpetgeo.2017.03.035.

Lai, J., G. Wang, Z. Fan, Z. Wang, J. Chen, Z. Zhou, S. Wang, and C. Xiao, 2018a, Corrigendum to "Fracture detection in oil-based drilling mud using a combination of borehole image and sonic logs" [JMPG: 84 (June 2017); pages 195–214]: Marine and Petroleum Geology, v. 96, 1 p., doi:10.1016/j.marpetgeo.2018.05.026.

Lai, J., G. Wang, S. Wang, J. Cao, M. Li, X. Pang, C. Han, et al., 2018b, A review on the applications of image logs in structural analysis and sedimentary characterization: Marine and Petroleum Geology, v. 95, p. 139–166, doi:10.1016/j.marpetgeo.2018.05.026.

Downloaded from http://pubs.geoscienceworld.org/aapgbull/article-pdf/105/11/2263/5431410/bltn19135.pdf
by China University of Geosciences Beijing user

Lai, J., S. Wang, G. Wang, Y. Shi, T. Zhao, X. Pang, X. Fan, Z. Qin, and X. Fan, 2019b, Pore structure and fractal characteristics of Ordovician Majiagou carbonate reservoirs in Ordos Basin, China: AAPG Bulletin, v. 103, no. 11, p. 2573–2596, doi:10.1306/02251917173.

Lai, J., S. Wang, C. Zhang, G. Wang, Q. Song, X. Chen, K. Yang, and C. Yuan, 2020, Spectrum of pore types and networks in the deep Cambrian to Lower Ordovician dolostones in Tarim Basin, China: Marine and Petroleum Geology, v. 112, p. 104081, doi:10.1016/j.marpetgeo.2019.104081.

Laubach, S. E., 2003, Practical approaches to identifying sealed and open fractures: AAPG Bulletin, v. 87, no. 4, p. 561–579, doi:10.1306/11060201106.

Li, Q., Z. Jiang, W. Hu, X. You, G. Hao, J. Zhang, and X. Wang, 2016, Origin of dolomites in the Lower Cambrian Xiaoerbulak Formation in the Tarim basin, NW China: Implications for porosity development: Journal of Asian Earth Sciences, v. 115, p. 557–570, doi:10.1016/j.jseaes.2015.10.022.

Loucks, R. G., 1999, Paleocave carbonate reservoirs; origins, burial-depth modifications, spatial complexity, and reservoir implications: AAPG Bulletin, v. 83, no. 11, p. 1795–1834.

Lu, X., Y. Wang, F. Tian, X. Li, D. Yang, T. Li, Y. Lv, and X. He, 2017, New insights into the carbonate karstic fault system and reservoir formation in the southern Tahe area of the Tarim basin: Marine and Petroleum Geology, v. 86, p. 587–605, doi:10.1016/j.marpetgeo.2017.06.023.

Lü, X., Y. Wang, H. Yu, and Z. Bai, 2017, Major factors affecting the closure of marine carbonate caprock and their quantitative evaluation: A case study of Ordovician rocks on the northern slope of the Tazhong uplift in the Tarim basin, western China: Marine and Petroleum Geology, v. 83, p. 231–245, doi:10.1016/j.marpetgeo.2017.03.006.

Luczaj, J. A., W. B. Harrison, and N. S. Williams, 2006, Fractured hydrothermal dolomite reservoirs in the Devonian Dundee formation of the central Michigan basin: AAPG Bulletin, v. 90, no. 11, p. 1787–1801, doi:10.1306/06270605082.

Lyu, W., L. Zeng, Z. Liu, G. Liu, and K. Zu, 2016, Fracture responses of conventional logs in tight–oil sandstones: A case study of the Upper Triassic Yanchang Formation in southwest Ordos Basin, China: AAPG Bulletin, v. 100, no. 9, p. 1399–1417, doi:10.1306/04041615129.

Lyu, W., L. Zeng, B. Zhang, F. Miao, P. Lyu, and S. Dong, 2017, Influence of natural fractures on gas accumulation in the Upper Triassic tight gas sandstones in the northwestern Sichuan Basin, China: Marine and Petroleum Geology, v. 83, p. 60–72, doi:10.1016/j.marpetgeo.2017.03.004.

Mollajan, A., and H. Memarian, 2016, Rock physics-based carbonate pore type identification using Parzen classifier: Journal of Petroleum Science Engineering, v. 145, p. 205–212, doi:10.1016/j.petrol.2016.03.021.

Moore, C. H., and W. J. Wade, 2013, Carbonate reservoirs: Porosity and diagenesis in a sequence stratigraphic framework: Amsterdam, Elsevier, Developments in Sedimentology, v. 67, 392 p.

Nabawy, B. S., 2013, Impacts of dolomitization on the petrophysical properties of El-Halal Formation, North Sinai, Egypt: Arabian Journal of Geosciences, v. 6, no. 2, p. 359–373, doi:10.1007/s12517-011-0369-5.

Ngia, N.R., M. Hu, D. Gao, 2019, Tectonic and geothermal controls on dolomitization and dolomitizing fluid flows in the Cambrian-Lower Ordovician carbonate successions in the western and central Tarim Basin, NW China: Journal of Asian Earth Sciences, v. 172, p. 359–382.

Nian, T., Z. Jiang, G. Wang, C. Xiao, W. He, L. Fei, and Z. He, 2018, Characterization of braided river-delta facies in the Tarim Basin Lower Cretaceous: Application of borehole image logs with comparative outcrops and cores: Marine and Petroleum Geology, v. 97, p. 1–23, doi:10.1016/j.marpetgeo.2018.06.024.

Nian, T., G. Wang, and H. Song, 2017, Open tensile fractures at depth in anticlines: A case study in the Tarim basin, NW China: Terra Nova, v. 29, no. 3, p. 183–190, doi:10.1111/ter.12261.

Pang, H., J. Chen, X. Pang, K. Liu, L. Liu, C. Xiang, and S. Li, 2013, Analysis of secondary migration of hydrocarbons in the Ordovician carbonate reservoirs in the Tazhong uplift, Tarim Basin, China: AAPG Bulletin, v. 97, no. 10, p. 1765–1783, doi:10.1306/04231312099.

Pires, L. O., A. Winter, and O. V. Trevisan, 2019, Dolomite cores evaluated by NMR: Journal of Petroleum Science Engineering, v. 176, p. 1187–1197, doi:10.1016/j.petrol.2018.06.026.

Qiu, N. S., J. Chang, Y. Zuo, J. Wang, and H. Li, 2012, Thermal evolution and maturation of lower Paleozoic source rocks in the Tarim Basin, northwest China: AAPG Bulletin, v. 96, no. 5, p. 789–821, doi:10.1306/09071111029.

Rajabi, M., S. Sherkati, B. Bohloli, and M. Tingay, 2010, Subsurface fracture analysis and determination of in-situ stress direction using FMI logs: An example from the Santonian carbonates (Ilam Formation) in the Abadan Plain, Iran: Tectonophysics, v. 492, no. 1–4, p. 192–200, doi:10.1016/j.tecto.2010.06.014.

Roth, S., B. Biswal, G. Afshar, R. J. Held, P. Øren, L. I. Berge, and R. Hilfer, 2011, Continuum-based rock model of a reservoir dolostone with four orders of magnitude in pore sizes: AAPG Bulletin, v. 95, no. 6, p. 925–940, doi:10.1306/12031010092.

Shen, A., W. Zhao, A. Hu, M. She, Y. Chen, and X. Wang, 2015, Major factors controlling the development of marine carbonate reservoirs: Petroleum Exploration and Development, v. 42, no. 5, p. 597–608, doi:10.1016/S1876-3804(15)30055-0.

Shen, A., J. Zheng, Y. Chen, X. Ni, and L. Huang, 2016, Characteristics, origin and distribution of dolomite reservoirs in Lower-Middle Cambrian, Tarim Basin, NW China: Petroleum Exploration and Development, v. 43, no. 3, p. 375–385, doi:10.1016/S1876-3804(16)30044-1.

Tian, F., X. Luo, and W. Zhang, 2019, Integrated geological-geophysical characterizations of deeply buried fractured-vuggy carbonate reservoirs in Ordovician strata, Tarim Basin: Marine and Petroleum Geology, v. 99, p. 292–309, doi:10.1016/j.marpetgeo.2018.10.028.

Downloaded from http://pubs.geoscienceworld.org/aapgbull/article-pdf/105/11/2263/5431410/bltn19135.pdf
by China University of Geosciences Beijing user

Tian, F., W. Wang, N. Liu, J. Jiang, C. Niu, Y. Zhang, and Y. Li, 2018, Rock-type definition and pore characterization of tight carbonate rocks based on thin sections and MICP and NMR experiments: Applied Magnetic Resonance, v. 49, no. 7, p. 631–652, doi:10.1007/s00723-018-0993-2.

Wang, Q., T. Nishidai, and M. P. Coward, 1992, The Tarim basin, NW China: Formation and aspects of petroleum geology: Journal of Petroleum Geology, v. 15, no. 1, p. 5–34, doi:10.1111/j.1747-5457.1992.tb00863.x.

Wang, S., Y. Cao, D. Du, S. Wang, H. Li, H. Dong, W. Yan, and Y. Bai, 2018, The characteristics and main controlling factors of dolostone reservoir in Lower Cambrian Xiaoerbulak Formation in Keping-Bachu area, Tarim Basin, NW China [in Chinese with English abstract]: Natural Gas Geoscience, v. 29, no. 6, p. 784–795.

Wang, Z. M., H. Xie, Y. Chen, Y. Qi, and K. Zhang, 2014, Discovery and exploration of Cambrian subsalt dolomite original hydrocarbon reservoir at Zhongshen-1 well in Tarim Basin [in Chinese with English abstract]: Zhongguo Shiyou Kantan, v. 19, p. 1–13.

Warren, J., 2000, Dolomite: Occurrence, evolution and economically important associations: Earth-Science Reviews, v. 52, no. 1–3, p. 1–81, doi:10.1016/S0012-8252(00)00022-2.

Wen, H., L. Wen, H. Chen, R. Zheng, L. Dang, and Y. Li, 2014, Geochemical characteristics and diagenetic fluids of dolomite reservoirs in the Huanglong Formation, Eastern Sichuan Basin, China: Petroleum Science, v. 11, no. 1, p. 52–66, doi:10.1007/s12182-014-0317-6.

Wierzbicki, R., J. J. Dravis, I. Al-Aasm, and N. Harland, 2006, Burial dolomitization and dissolution of Upper Jurassic Abenaki platform carbonates, Deep Panuke reservoir, Nova Scotia, Canada: AAPG Bulletin, v. 90, no. 11, p. 1843–1861, doi:10.1306/03200605074.

Wilson, M. E. J., M. J. Evans, N. H. Oxtoby, D. S. Nas, T. Donnelly, and M. Thirlwall, 2007, Reservoir quality, textural evolution, and origin of fault-associated dolomites: AAPG Bulletin, v. 91, no. 9, p. 1247–1272, doi:10.1306/05070706052.

Wilson, T. H., V. Smith, and A. Brown, 2015, Developing a model discrete fracture network, drilling, and enhanced oil recovery strategy in an unconventional naturally fractured reservoir using integrated field, image log, and three-dimensional seismic data: AAPG Bulletin, v. 99, no. 4, p. 735–762, doi:10.1306/10031414015.

Worden, R. H., P. C. Smalley, and M. M. Cross, 2000, The influence of rock fabric and mineralogy on thermochemical sulfate reduction: Khuff Formation, Abu Dhabi: Journal of Sedimentary Research, v. 70, no. 5, p. 1210–1221, doi:10.1306/110499701210.

Xu, C., T. P. Cronin, T. E. McGinness, and B. Steer, 2009, Middle Atokan sediment gravity flows in the Red Oak field, Arkoma Basin, Oklahoma: A sedimentary analysis using electrical borehole images and wireline logs: AAPG Bulletin, v. 93, no. 1, p. 1–29, doi:10.1306/09030808054.

You, X. L., S. Sun, and J. Zhu, 2014, Significance of fossilized microbes from the Cambrian stromatolites in the Tarim Basin, Northwest China: Science China. Earth Sciences, v. 57, no. 12, p. 2901–2913, doi:10.1007/s11430-014-4935-z.

You, X. L., S. Sun, J. Q. Zhu, Q. Li, W. Hu, and H. Dong, 2013, Microbially mediated dolomite in Cambrian stromatolites from the Tarim Basin, north-west China: Implications for the role of organic substrate on dolomite precipitation: Terra Nova, v. 25, no. 5, p. 387–395, doi:10.1111/ter.12048.

Zeng, L., 2010, Microfracturing in the Upper Triassic Sichuan Basin tight-gas sandstones: Tectonic, overpressure, and diagenetic origins: AAPG Bulletin, v. 94, no. 12, p. 1811–1825, doi:10.1306/06301009191.

Zeng, L. B., and X. Li, 2009, Fractures in sandstone reservoirs with ultra-low permeability: A case study of the Upper Triassic Yanchang Formation in the Ordos basin, China: AAPG Bulletin, v. 93, no. 4, p. 461–477, doi:10.1306/09240808047.

Zhang, H., Z. Cai, F. Hao, L. Qi, L. Yun, and L. Jiang, 2018, Hydrogeomorphologic architecture of epikarst reservoirs in the Middle-Lower Ordovician, Tazhong Uplift, Tarim Basin, China: Marine and Petroleum Geology, v. 98, p. 146–161, doi:10.1016/j.marpetgeo.2018.08.008.

Zhang, J., W. Hu, Y. Qian, X. Wang, J. Cao, J. Zhu, Q. Li, and X. Xie, 2009, Formation of saddle dolomites in Upper Cambrian carbonates, western Tarim basin (northwest China): Implications for fault-related fluid flow: Marine and Petroleum Geology, v. 26, no. 8, p. 1428–1440, doi:10.1016/j.marpetgeo.2009.04.004.

Zhao, W. Z., A. Shen, A. Hu, J. Zhou, and X. Ni, 2015, A discussion on the geological background of marine carbonate reservoirs development in Tarim, Sichuan and Ordos Basin, China [in Chinese with English abstract]: Yanshi Xuebao, v. 31, no. 11, p. 3495–3508.

Zhao, W. Z., A. Shen, S. Hu, W. Pan, J. Zheng, and Z. Qiao, 2012, Types and distributional features of Cambrian-Ordovician dolostone reservoirs in Tarim Basin, northwestern China [in Chinese with English abstract]: Yanshi Xuebao, v. 28, no. 3, p. 758–768.

Zhao, W. Z., A. Shen, J. Zhou, X. Wang, and J. Lu, 2014, Types, characteristics, origin and exploration significance of reef-shoal reservoirs: A case study of Tarim Basin, NW China and Sichuan Basin, SW China: Petroleum Exploration and Development, v. 41, no. 3, p. 283–293, doi:10.1016/S1876-3804(14)60034-3.

Zheng, J., A. Shen, Y. Chen, X. Ni, and X. Zhang, 2015, Reservoir space and reservoir classification of Lower Paleozoic dolomite in the Tarim Basin [in Chinese with English abstract]: Natural Gas Geoscience, v. 26, no. 7, p. 1256–1267.

Zheng, J. F., A. Shen, Y. Liu, and Y. Chen, 2012, Multi-parameter comprehensive identification of the genesis of Lower Paleozoic dolomite in Tarim Basin, China [in Chinese with English abstract]: Acta Petrolei Sinica, v. 33, no. S2, p. 145–153.

Downloaded from http://pubs.geoscienceworld.org/aapgbull/article-pdf/105/11/2263/5431410/bltn19135.pdf
by China University of Geosciences Beijing user

Zheng, J. F., A. Shen, Z. Qiao, and X. Ni, 2013, Genesis of dolomite and main controlling factors of reservoir in Penglaiba Formation of Lower Ordovician,Tarim Basin: A case study of Dabantage outcrop in Bachu area [in Chinese with English abstract]: Yanshi Xuebao, v. 29, no. 9, p. 3223–3232.

Zhu, D., Q. Meng, Z. Jin, and W. Hu, 2015a, Fluid environment for preservation of pore spaces in a deep dolomite reservoir: Geofluids, v. 15, no. 4, p. 527–545, doi:10.1111/gfl.12123.

Zhu, D., Q. Meng, Z. Jin, Q. Liu, and W. Hu, 2015b, Formation mechanism of deep Cambrian dolomite reservoirs in the Tarim basin, northwestern China: Marine and Petroleum Geology, v. 59, p. 232–244, doi:10.1016/j.marpetgeo.2014.08.022.

Zhu, G., F. Chen, M. Wang, Z. Zhang, R. Ren, and L. Wu, 2018, Discovery of the lower Cambrian high-quality source rocks and deep oil and gas exploration potential in the Tarim Basin, China: AAPG Bulletin, v. 102, no. 10, p. 2123–2151, doi:10.1306/03141817183.

Zhu, G., H. Wang, and N. Weng, 2016, TSR-altered oil with high-abundance thiaadamantanes of a deepburied Cambrian gas condensate reservoir in Tarim Basin: Marine and Petroleum Geology, v. 69, p. 1–12, doi:10.1016/j.marpetgeo.2015.10.007.

Downloaded from http://pubs.geoscienceworld.org/aapgbull/article-pdf/105/11/2263/5431410/bltn19135.pdf
by China University of Geosciences Beijing user